Activation and Safety Analysis for Advanced Fuel Fusion Reactors

H.Y. Khater

March 1991

UWFDM-849

Ph.D. thesis.

FUSION TECHNOLOGY INSTITUTE

UNIVERSITY OF WISCONSIN

MADISON WISCONSIN

Activation and Safety Analysis for Advanced Fuel Fusion Reactors

H.Y. Khater

Fusion Technology Institute
University of Wisconsin
1500 Engineering Drive
Madison, WI 53706

http://fti.neep.wisc.edu

March 1991

UWFDM-849

Ph.D. thesis.

ACTIVATION AND SAFETY ANALYSIS FOR ADVANCED FUEL FUSION REACTORS

by

Hesham Youssef Khater

A thesis submitted in partial fulfillment of the

requirements for the degree of

Doctor of Philosophy

(Nuclear Engineering and Engineering Physics)

at the

University of Wisconsin - Madison

1990

ACTIVATION AND SAFETY ANALYSIS FOR ADVANCED FUEL FUSION REACTORS

Hesham Youssef Khater

Under the supervision of Professor William Ferdinand Vogelsang

A D-^{3}He reactor has the potential to be an inherently safer fusion reactor due to the fact that most of the energy released in the plasma would be in the form of protons rather than neutrons. Even though most protons thermalize on the background plasma, a small fraction of them would follow orbits which strike the reactor structure. When protons strike the first wall, nuclear reactions may be induced resulting in the production of radioactive isotopes.

Until recently, activation analyses of D-^{3}He fusion reactors have focused on the radioactivity induced by neutrons produced from the D-D and D-T secondary reactions. Proton interaction with structural materials presents a potential source of induced radioactivity that has been ignored due to the general lack of cross section data for proton interactions with different target elements and the expectation that it would be significantly smaller than the radioactivity induced by neutrons. A computer program PTTY has been developed to produce a proton thick-target yield library. A wide range of experimental radionuclide production cross sections have been collected for protons with energies similar to those protons produced in a D-^{3}He fusion

reactor. Proton energy-dependent cross sections ($E_p \leq 14.7$ MeV) were used along with the proton stopping data of Anderson and Ziegler to produce the proton-induced thick-target radionuclide activation yield library. In its present form, the library contains thick-target yield data for 164 radioactive isotopes. Even though most of the available cross sections for protons with energy ≤ 14.7 MeV were those of (p,n) reactions, some cross sections for (p,γ), (p,2n), (p,α) and (p,pn) reactions were found and used in the calculations. The library is linked to a second computer program PIAC that calculates proton-induced radioactivity. Another potential source of radioactivity which has also been considered is the activity induced by neutrons produced from proton interactions with the reactor structure through (p,n) reactions. A computer program PNNES that evaluates the energy spectrum of these neutrons has been developed. The program produces a neutron flux in a 46 neutron energy group structure.

PNNES, PIAC and the thick-target yield library have been used in an activation analysis study aimed at investigating the effect of proton-induced activity on the total level of radioactivity generated in Apollo-L2 (a D-^{3}He tokamak fusion power reactor). Because protons have a short range in solid targets, their effect has been noticed only within the first wall of the reactor.

Acknowledgement

I would like to dedicate this thesis to the memory of my father as one of the least things I can do to acknowledge his vital role in my life. I would also wish to thank the rest of my family for all the love and support they have given me every step of the way.

I deeply appreciate the patience and support of Prof. William Vogelsang throughout this thesis work. Many thanks are due to Dr. Mohamed Sawan and Makarem Hussein for their continuous and never ending support. I also wish to express my gratitude to my colleagues Mohamed Elafify, Tsutomu Tanaka, Arthur Bennethum, Nermine Ramadan, Osman Yasar and Stephen Lomperski for their friendship. I am indebted to Kathy Moulton for her invaluable and timely support.

Finally, I wish to acknowledge the assistance and support of all the members of the Fusion Technology Institute design team, especially Prof. Gerald Kulcinski, Dr. John Sanatrius and Dennis Bruggink for their encouragement and many constructive suggestions.

Contents

List of Figures

List of Tables

Chapter 1

Introduction

One of the main goals in the design of fusion reactors is to achieve as clean an environment as possible. It has always been thought that the radiological hazard associated with fusion reactors should present fewer potential difficulties than those associated with existing fission reactors.

Many activation analysis studies on different fusion reactor designs utilizing several fuel cycles have been conducted. The most commonly considered fuel cycles are Deuterium-Tritium (D-T), Deuterium-Deuterium (D-D) and Deuterium-Helium (D-^{3}He). The three fuel cycles have the following primary reactions:

$$D + T \longrightarrow {}^4He(3.52MeV) + n(14.07MeV) \tag{1.1}$$

$$D + D \longrightarrow {}^3He(0.82MeV) + n(2.45MeV) \tag{1.2}$$

$$D + D \longrightarrow T(1.01MeV) + p(3.03MeV) \tag{1.3}$$

and

$$D + {}^3He \longrightarrow {}^4He(3.67MeV) + p(14.67MeV) \qquad (1.4)$$

Up to recently, most of the fusion reactor designs have concentrated on the D-T fuel cycle because of the following reasons:

1. It has the lowest ignition temperature of the three fuel cycles.
2. High reaction rate.
3. Fuel availability.

However, the D-T fuel cycle has several disadvantages. In particular:

- 80 % of the reaction energy is carried by 14.1 MeV neutrons.
- The need to control a large amount of radioactive tritium.
- The permanent need to contain lithium in the blanket for the purpose of breeding tritium.

The 14.1 MeV neutrons cause severe radiation damage to the blanket and shield structure and induce a significant amount of radioactivity in the surrounding structural materials.

Recently, attention has been given to alternative fuel cycles, especially the D-^{3}He fuel cycle. A D-^{3}He reactor has the potential to be an inherently safer fusion reactor due to the fact that most of the energy released in the

plasma would be in the form of charged particles (protons) rather than neutrons. So far, activation analyses of D-^{3}He fusion reactors have only focused on the radioactivity induced by neutrons produced from the D-D and D-T secondary reactions (equations (1.1) and (1.2)). Such neutrons represent the majority of the neutron population expected to exist in a D-^{3}He fusion reactor. However, a much smaller fraction of secondary neutrons is produced by proton interactions with the different structural materials in the reactor.

Calculations of radioactivity induced by both protons and secondary neutrons produced by proton interactions with the structural materials are needed to enhance our understanding of the safety problems that might be associated with D-^{3}He fusion reactors.

The question of the level of radioactivity produced by proton interactions with the structural materials is addressed in chapter three. A method to calculate the proton-induced radioactivity through the use of proton thick-target yields is presented. Experimental cross section data from the literature were used to develop a proton-induced thick-target radionuclide activation yield library. In chapter four a technique to evaluate the energy spectrum of neutrons produced from (p,n) reactions by using the multigroup transfer matrices method is described. A case study of a D-^{3}He tokamak fusion reactors (Apollo-L2) is investigated in chapter five. A detailed activity and safety analysis is performed and a comparison between proton-induced and neutron-induced activities is presented. The analysis includes a radwaste

classification, biological dose rate calculation and investigation of the thermal response of the reactor shield following a loss of coolant accident (LOCA). Finally, conclusions and suggestions for future work are included in the final chapter of this thesis.

Chapter 2

Activation Analysis Background

2.1 Previous Activation Studies

In the early years of activation analysis, the main emphasis was focused on the neutron-induced activity associated with the D-T fuel cycle. Fraas and Postma [1] conducted a preliminary assessment of the hazard problems associated with a D-T fusion reactor. They considered tritium to be the principal source of radiological hazard. Although tritium is produced at a rate of from 10^3 to 10^5 times that in fission reactors, it is burned as a fuel at a high rate such that the total tritium inventory for a fusion reactor would be within a factor of 100 or less of that for a fission reactor for a given power output. They showed that, for 5000 MW_t fusion reactor power plant, the afterheat immediately following shutdown is about 0.2 % of the full power

output.

Steiner [2] calculated the activity and decay power for a niobium structure of 5000 MW_t reactor blanket. After 10 years of operation, the activity was about 2×10^{10} Curies and the decay power was about 50 MW. He analyzed several cross sections of ^{93}Nb and reached the conclusion that only radioactive isotopes of ^{93}Nb produced as a result of (n,2n), (n,γ) and (n,n$'$), nuclear reactions (see Fig. (2.1)dominate the produced activity.

In a later paper, Steiner [3] compared the values of the induced activity and decay power for the niobium structure of a fusion reactor blanket with values observed for the spent fuel of a fission reactor. He concluded that the activity in Curie per Watt of thermal power is comparable for the niobium structure and the spent fuel, and that the fractional decay power associated with the niobium structure is about 15 % of that associated with the spent fuel. He also compared the D-T, D-D and D-^{3}He fuel cycles on the basis of neutron irradiation effects and environmental considerations, and stated that comparable amounts of neutrons and tritium are generated in each fuel cycle. In conclusion the following observations were made:

- The induced activity and decay power are comparable in each fuel cycle.
- The problems of tritium containment must be considered in each fuel cycle.

Dudziak [4] calculated the afterheat in the niobium blanket of 2000 MW_t

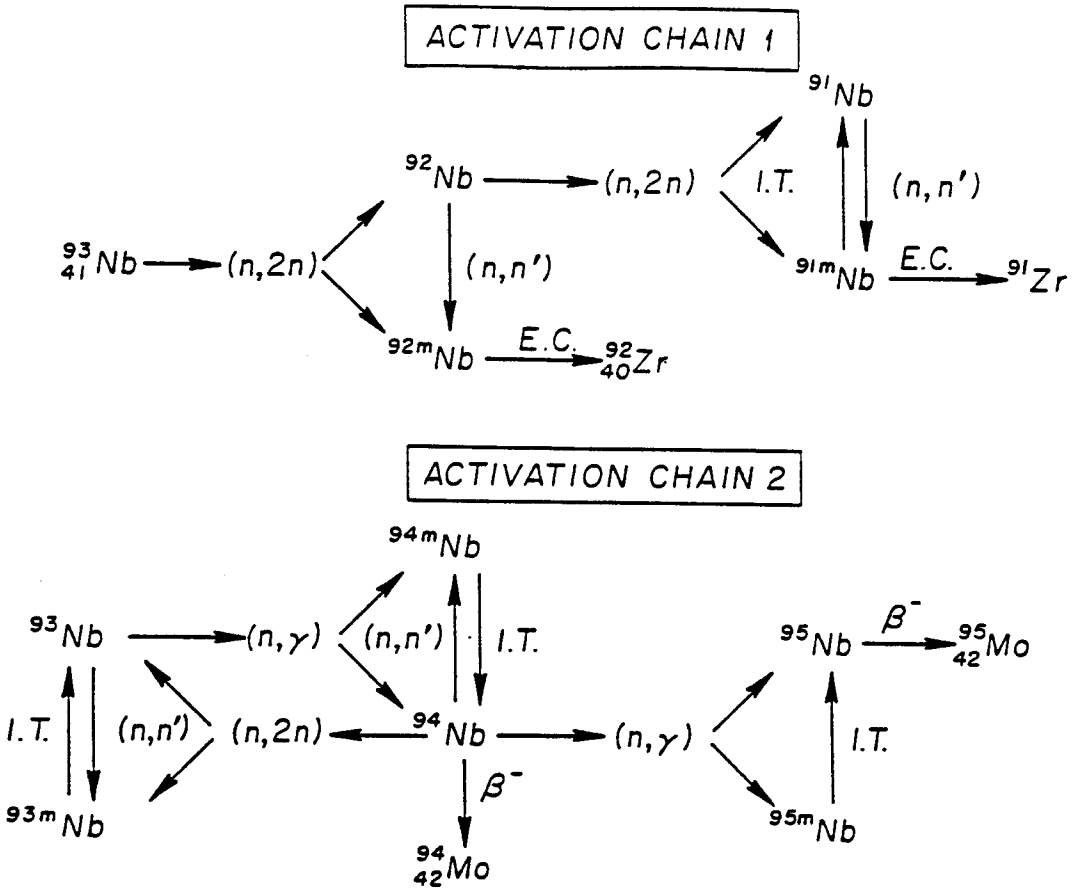

Figure 2.1: Niobium Activation Chains.

reactor. Molybdenum was mentioned as possible choice as a blanket but it was indicated that a large amount of afterheat would be produced due to the large 14.1 MeV cross section of molybdenum.

Steiner and Fraas [5] studied using vanadium as alternate structural material. They compared the estimated quantities of the principal radioactive inventories, the long-lived activities and the afterheat for a reference fusion reactor blanket structure (niobium or vanadium) with those for an advanced fission reactor.

In the conceptional design of the blanket and shield region for a toroidal fusion reactor [6], Fraas calculated the afterheat to be about 0.25 % of the design power output, or about 10 % of that for a comparable fission reactor one minute after shutdown.

In a study of a minimum activity blanket [7] Powell *et al.* considered the use of SAP, a pure aluminum strengthened by an Al_2O_3 dispersoid, as a structural material. The results showed that after 30 years of operation, short lived activities were dominated by ^{24}Na ($T_{1/2}$ = 15 hours) which decay to a negligible amount in a few days, leaving a long lived inventory of about 10^4 Curies/1000 MW_e (principally ^{26}Al ($T_{1/2} = 7.3 \times 10^5$ years)). The conclusion was that the SAP does not present a problem of permanent waste disposal.

In a later study [8], Powell *et al.* conducted another study of a low residual radioactivity aluminum blanket. The long-lived residual radioactivity in the

blanket was six to seven orders of magnitude lower than that of niobium or stainless steel structure. Assuming 3 years of reactor operation before shutdown, the residual radioactivity in the blanket 10 years after shutdown was about 1000 Curies and was mostly produced by ^{26}Al.

Kulcinski, Lott and Yang [9] calculated the transmutation rates for three structural materials, 316 stainless steel, V-20Ti and Nb-1Zr. They concluded that regarding metallic transmutations, V-20Ti presents no problem for wall loadings less than 10 MW/m^2, 316 stainless steel undergoes no significant changes at 0.5 MW/m^2, but is considerably altered at 10 MW/m^2 and Nb-1Zr is limited to wall loadings below 3 MW/m^2. An activation analysis was conducted for the previous study by Vogelsang *et al.* [10] for the same three structural materials. The results showed that V-20Ti produces the least radioactivity and afterheat.

Price *et al.* [11] compared the results obtained from several fusion reactor design studies. The study concluded that:

1. Fusion reactor blanket induced radioactivity at shutdown is in the range of 0.1 to 5 Ci/W$_t$.

2. Fusion reactor afterheat at shutdown is in the range of 0.1 to 1 % of the design power.

3. Vanadium is a very attractive material from the waste disposal standpoint, while niobium blankets are the worst because of the production

of long lived ^{94}Nb.

Dudziak and Krakowski [12] calculated the induced radioactivity and afterheat for the theta-pinch reactor (RTPR) structural material (Nb-1Zr and V-20Ti) and compared their results with those reported for other fusion reactors and typical fast fission reactors. The study showed that V-20Ti structure induce an order of magnitude less short-term radioactivity relative to Nb-1Zr structure, and a negligible long-term activity. In comparing fusion and fission reactors, they stated that both types of reactors may induce comparable radioactivity [Ci/W$_t$]. But for fusion reactors, afterheat power densities are about two orders of magnitude lower than for fission reactors.

Several fusion reactor ISSEC (Internal Spectral Shifter and Energy Converter) blanket concepts were introduced by Conn *et al.* [13]. The blanket designs were based on the idea of shifting or softening the neutron spectrum incident on the first structural wall. In turn, the softened neutron spectrum reduces radioactivity and afterheat levels.

A comparison between the induced radioactivity, afterheat and biological hazard potential (BHP) in UWMAK-I (316 stainless steel), PPPL (PE-16), ORNL (Nb), LLL (316 stainless steel) and BNL (SAP) blankets were conducted by Conn, Sung and Abdou [14]. The radioactivity levels at shutdown after two years of operation were within a factor of four of each other and were clustered at about 10^6 Ci/MW$_t$. The BNL (SAP) blanket proved to be

the best from the viewpoint of long-term radioactivity, while the ORNL (Nb) blanket was the worst. The ORNL (Nb) blanket had the lowest afterheat at shutdown and the BHP values of the BNL (SAP) blanket became very small in several weeks after shutdown. The afterheat power density in any of the five blankets was found to be a factor of 10 to 60 less than the afterheat power density in fast breeder reactors.

In a different comparison study [15], Williams, Santoro and Gabriel compared the neutron-induced radioactivity and afterheat of niobium, 304 stainless steel and nimonic-105 structural materials in a conceptual D-T fusion reactor blanket model. At shutdown, the activity in the 304 stainless steel blanket was a factor of four lower than both the niobium and nimonic-105 blankets. The afterheat at one day after shutdown in the nimonic-105 blanket was 35 % and 65 % larger than in the niobium and 304 stainless steel blankets, respectively.

Vogelsang's [16] calculations for various fusion reactor designs with a selection of various structural materials showed that:

- At shutdown, radioactivity ranges from 5100 Ci/kW$_t$ for Nb-1Zr to 750 Ci/kW$_t$ for 2024 Al.

- In the period of time following shutdown, the V-20Ti and 2024 Al have an advantage in either radioactivity or afterheat over TZM, 316 stainless steel or Nb-1Zr.

- All materials except V-20Ti have long half-life contributors.

Cheng, Sung and Sze [17] considered a gas-carried lithium oxide cooling-breeding fusion reactor blanket. The calculated radioactivity and afterheat after shutdown were found to be comparable to the 316 stainless-steel structured UWMAK-I design.

Conn, Okula and Johnson [18] conducted a study aiming to minimize radioactivity by elemental and isotopic tailoring of materials for fusion reactors. They considered both 316 stainless steel and TZM. They found that the principles of both elemental substitution and isotopic tailoring can reduce the long-term radioactivity levels by orders of magnitude compared to normal type 316 stainless steel.

Youssef and Conn [19] studied the induced radioactivity, afterheat and BHP levels in the D-D fuel cycle fusion reactor SATYR. The study was conducted for both ferritic steel (HT-9) and sintered aluminum product (SAP) structural materials. Results were compared to the corresponding levels in the D-T fuel cycle reactors STARFIRE and WITAMIR-I. They concluded that:

1. The long-term levels of radioactivity, afterheat and BHP in the HT-9 structure of the D-D reactor are higher by a factor of 2 to 6 than those found in D-T reactors.

2. Very small radioactivity levels were obtained within weeks after shut-

down when SAP was used as a structural material.

3. The D-D reactors permit simpler blanket designs by eliminating tritium breeding as a part of the blanket function.

4. Replacing both molybdenum and nickel in the steel composition with vanadium leads to several orders of magnitude reduction in the long term radioactivity levels.

Most recently, several studies of different blanket concepts for the International Thermonuclear Experimental Reactor (ITER) were conducted. Attaya, Gohar, Smith and Baker [20] conducted an activation analysis for the inboard shield of the ITER design option utilizing water cooled solid breeder blanket. They examined both the austenitic steel stabilized with nickel (Ni-SS) and the austenitic steel stabilized with manganese (Mn-SS) as structure materials. The results showed that the long-term activation problems of Mn-SS are much less than of Ni-SS. Mn-SS structure can qualify as class C low level waste, while Ni-SS structure can not qualify for near surface burial.

In another study Khater, Sawan, Lomperski and Sviatoslavsky [21] performed an activation analysis for the outboard and inboard blanket and shield of an ITER design option utilizing an aqueous lithium salt blanket. The option of using PCA stainless steel or a low activation austenitic steel (Tenelon) as structural materials was assessed. The long-term activation problems of

Tenelon were less than that of PCA. A Tenelon structure resulted in about 50 % more decay heat generation in the first day after shutdown compared to the PCA structure, but both structures produced comparable integrated decay heat in one week after shutdown.

Vogelsang and Khater [22] studied the impact of D-^{3}He fusion reactors on waste disposal. In the study, two austenitic stainless steels (PCA and Tenelon), two ferritic alloys (HT-9 and modified HT-9) and a vanadium alloy (V-15Cr-5Ti) were considered. The study was conducted for both tokamak and tandem mirror fusion reactors. The V-15Cr-5Ti alloy showed the lowest long-term activity level, while the PCA alloy showed the highest level. Modified HT-9, Tenelon and V-15Cr-5Ti alloys qualified as class A or C low level waste.

In the study of a high efficiency, D-^{3}He tandem mirror fusion reactor (Ra) [23], Santarius *et al.* stated that Ra would have significantly lower activation levels than a D-T reactor and that all of the structure components would qualify as class C low level waste.

Kulcinski *et al.* [24] presented a preconceptual design of a D-^{3}He tokamak fusion reactor. The high manganese austenitic stainless steel (Tenelon) was used as a structural material for the first wall, vacuum vessel and shield. The Tenelon structure for all components classified as class A low level waste within one year after shutdown.

2.2 Previous Radioactivity Codes

Many radioactivity codes have been developed for the calculation of neutron-induced radioactivity in fusion reactors. In this section a brief description will be given for some of the widely used radioactivity codes.

2.2.1 The RACC Code

The computational algorithm in RACC [25] is based on Gear's stiffly stable matrix method. The implicit assumption made in deriving the transmutation equation of an isotope is that neutron group fluxes remain constant at each spatial point over the time span in question. The time rate of change of the number density of nuclei over a time interval from t_o to t can be written as:

$$\frac{d\vec{N}}{dt} = A\vec{N}(t) + \vec{S}(t) \tag{2.1}$$

with an initial condition:

$$\vec{N}(t_o) = \vec{N}_o, \tag{2.2}$$

where $\vec{N}(t)$ and $\vec{S}(t)$ are two vectors which represent the different atomic numbers and external source densities of all isotopes at any time t, respectively. The elements a_{ij} of the matrix $A = \{a_{ij}\}$ are given by

$$a_{ij} = -(\hat{\sigma}_i^D + \lambda_i)\delta_{ij} + (\hat{\sigma}_{j\to i}^F + \lambda_j b_{j\to i}) \tag{2.3}$$

Here

$\hat{\sigma}_i^D$ = $\int \phi(E)\sigma_i^D(E)dE$,

λ_i = decay constant of isotope i ,

δ_{ij} = Kronecker delta ,

$\hat{\sigma}_{j\to i}^F$ = $\int \phi(E)\sigma_{j\to i}^F(E)dE$,

$b_{j\to i}$ = branching ratio of decay from isotope j to isotope i.

as

$\phi(E)$ = neutron flux at energy E ,

$\sigma_i^D(E)$ = microscopic destruction cross section of isotope i at neutron energy E ,

$\sigma_{j\to i}^F(E)$ = microscopic cross section of isotope j leading to production of isotope i at neutron energy E.

The difference equation of the Gear method for equations (2.1) and (2.2) can be written as:

$$(\mathbf{I} - h\beta_o A)\vec{N}_n = \sum_{i=1}^{K} \alpha_i \vec{N}_{n-i} + h\beta_o \vec{S}_o \tag{2.4}$$

or

$$B\vec{N} = \vec{Q} \tag{2.5}$$

assuming that the external source is independent of time t. *i.e.*,

$$\vec{S}(t) = \vec{S}_o \tag{2.6}$$

In equation (2.4), α_i 's and $\beta_\circ$ are Gear's stiffly stable coefficients and **I** is an identity matrix. h and $\vec{N}_{n-i}$ are defined as:

$$h = t_n - t_{n-1} \tag{2.7}$$

$$\vec{N}_{n-i} = \vec{N}(t_{n-i}) \qquad 1 \leq i \leq K \tag{2.8}$$

The algorithm used to solve equation (2.4) is based on the matrix triangularization followed by Gaussian elimination for the system of equations described by equation (2.5).

RACCDLIB and RACCXLIB [26] are the two decay data and cross section libraries that are used with the RACC code. The two libraries are based on both the ENDF [27] and ENSDF [28] data libraries.

2.2.2 The REAC and REAC2 codes

The REAC2 code is a modification of the REAC [29] code which is based on the assumption that during any period of time (an irradiation time having constant flux followed by a cooling time with flux $\phi = 0$):

1. No reaction occurs on a reaction or decay product.

2. At most, two decays can occur for a reaction product or the initial isotope.

The transmutation of nuclides in the code is described by:

$$\frac{dN_i(t)}{dt} = (G_r + G_d) - (L_r + L_d) \tag{2.9}$$

where, G_r & G_d are two terms that describe the gain from reactions and decay, respectively, and L_r & L_d describe the loss due to reactions and decay, respectively. The terms G_r, G_d, L_r and L_d can be written as:

$$G_r = \phi(t) \sum_j N_j(t) \sigma_{j \to i}(t), \tag{2.10}$$

$$G_d = \sum_k \lambda_{k \to i} N_k(t), \tag{2.11}$$

$$L_r = \phi(t) N_i(t) \sum_l \sigma_{i \to l}(t), \tag{2.12}$$

and

$$L_d = N_i(t) \sum_m \lambda_{i \to m}. \tag{2.13}$$

where

$N_i(t)$ = number density of nuclide i ,

$\phi(t)$ = total flux ,

$\sigma_{n \to p}(t)$ = spectrum averaged microscopic cross section for changing nuclide n into nuclide p ,

$\lambda_{q \to r}$ = decay constant for nuclide q changing into nuclide r.

The code is run for a series of time periods to obtain the desired number densities of the different isotopes.

The REAC code uses a 63-group cross section library (FMITACTIVLIB) that is based on ENDF/B-V [30] library. The ENDF/B-V and the seventh edition of the table of isotopes were used as sources for the decay data library.

2.2.3 The ORIGEN, ORIGEN2 and FORIG codes

FORIG [32] is a modification of the ORIGEN2 [33] code, which is a revised version of the ORIGEN [34] code. The ORIGEN (ORNL isotope generation and depletion code) uses the matrix exponential method to solve a large system of coupled, linear, first-order ordinary differential equations with constant coefficients. The code solves an expression for the formation and disappearance of a nuclide by nuclear transmutation and radioactive decay, which may be written as:

$$\frac{dN_i}{dt} = \sum_{j=1}^{n} l_{ij}\lambda_j N_j + \bar{\phi}\sum_{k=1}^{n} f_{ik}\sigma_k N_k - (\lambda_i + \bar{\phi}\sigma_i)N_i \qquad (i = 1,2,\ldots,n) \qquad (2.14)$$

where

N_i = the atom density of nuclide i ,

λ_i = the radioactive disintegration constant for nuclide i ,

σ_i = the spectrum-averaged neutron absorption cross section of nuclide i ,

l_{ij}, f_{ik} = the fractions of radioactive disintegration and neutron absorption by nuclides which lead to the formation of nuclide i ,

$\bar{\phi}$ = the position and energy averaged neutron flux.

Assuming that the neutron flux is constant over short time intervals, equation (2.14) can be written as:

$$\dot{\vec{N}} = \vec{\vec{A}}\vec{N} + \vec{B} \tag{2.15}$$

where $\vec{\vec{A}}$ is a transition matrix containing the rate coefficients for radioactive decay and neutron capture. $\vec{N}$ and $\vec{B}$ are the number density and production vectors, respectively. Equation (2.15) has a solution which may be written in the form:

$$\vec{N} = \vec{N}(0)\left(\sum_{m=0}^{\infty}\frac{(\vec{\vec{A}}t)^m}{m!}\right) + \left(\sum_{m=0}^{\infty}\frac{(\vec{\vec{A}}t)^m}{(m+1)!}\right)\vec{B}t \tag{2.16}$$

where $\vec{N}(0)$ is the initial number density vector.

For long-lived nuclides, an expression for equation (2.16) as the sum of infinite series can be written for one nuclide as:

$$N_i(t) = \sum_{n=0}^{\infty} C_i^n + \sum_{n=1}^{\infty} D_i^n \tag{2.17}$$

where C_i^n and D_i^n are generated by the use of the following recursion relations:

$$C_i^{n+1} = \frac{t}{n+1}\sum_{j=1}^{n} a_{ij}C_j^n,$$

$$D_i^{n+1} = \frac{t}{n+1}\sum_{j=1}^{n} a_{ij}D_j^n.$$

where, $C_i^0 = N_i(0)$ and $D_i^1 = b_i t$. a_{ij} and b_i are elements of the transition matrix and production vector, respectively.

For short-lived nuclides having short-lived precursors, the code uses a generalized form of the Bateman equations which treat an arbitrary forward-branching chain. Bateman's solution for the i'th member in a chain at time t may be written as:

$$N_i(t) = N_i(0)e^{-d_i t} + \sum_{k=1}^{i-1} N_k(0) \prod_{n=k}^{i-1} \frac{a_{n+1,n}}{d_n} \left[\sum_{j=k}^{i-1} d_j \frac{e^{-d_j t} - e^{-d_i t}}{d_i - d_j} \prod_{\substack{n=k \\ n \neq j}}^{i-1} \frac{d_n}{d_n - d_j} \right] \tag{2.18}$$

where $\prod_{n=k}^{i-1} a_{n+1,n}$ is equal to the product of $a_{k+1,k}, a_{k+2,k+1}, \ldots, a_{i,i-1}$ and $d_i = -a_{i,i}$ is the removal constant of nuclide i.

For short-lived nuclides having long-lived precursors, the short-lived nuclide is assumed to be in seqular equilibrium with its parent at the end of any time interval, hence:

$$\dot{N}_i = 0 = \sum_{j=1}^{n} a_{ij} N_i + b_i \tag{2.19}$$

Equation (2.19) is solved by using the Gauss-Seidel iterative technique.

All of the three codes require flux-averaged cross section. So, different cross section libraries are required for different regions of any specific fusion reactor design. The ORLIB [35] code utilizes the ACTL [36] cross section library and the TART [37] neutronics code to produce a one-energy-group cross section library to be used with any region of a fusion reactor.

2.2.4 The DKR code

The DKR [38,40] uses the linear decay chain method to calculate radioactivity and related parameters in fusion reactors. The time rate of change of the number density of a nuclide k can be written as:

$$\frac{dN_k}{dt} = \sum_j \gamma_j^k N_j - \lambda_k N_k - N_k \int_0^\infty \sigma_a^k(E)\phi(E)dE \qquad (2.20)$$

where

γ_j^k = probability of forming nuclide k from nuclide j per unit time ,

λ_k = decay constant of nuclide k ,

σ_a^k = absorption cross section of nuclide k ,

$\phi(E)$ = energy dependent neutron flux.

In a linear decay chain, equation (2.20) takes the form:

$$\frac{dN_k}{dt} = \gamma_{k-1}^k N_{k-1} - \beta_k N_k \qquad (2.21)$$

where

γ_{k-1}^k = the production rate of nuclide k from its precursor ,

β_k = the destruction rate of nuclide k ,

N_{k-1} = number density of nuclide k precursor.

The solution of equation (2.21) can be written as:

$$N_k(t) = N_k(t_\circ)e^{-\beta_k(t-t_\circ)} + \gamma_{k-1}^k \sum_{j=1}^{k-1} \frac{a_j^{k-1}}{\beta_k - \beta_j}(e^{-\beta_j(t-t_\circ)} - e^{-\beta_k(t-t_\circ)}) \qquad (2.22)$$

where $N_k(t_o)$ is the initial number density of nuclide k.

The coefficients are generated by the use of the following recursion relations:

$$a_k^k = N_k(t_o) - \gamma_{k-1}^k \sum_{j=1}^{k-1} \frac{a_j^{k-1}}{\beta_k - \beta_j}, \tag{2.23}$$

and

$$a_j^k = \gamma_{k-1}^k \frac{a_j^{k-1}}{\beta_k - \beta_j} \qquad j = 1, 2, \ldots, k-1. \tag{2.24}$$

There are two versions of the DKR code. The older version [38] uses the DCDLIB [39] cross section and decay data library. The newer version [40] uses the ACTL library. The DKR code prepares a gamma source file that can be used by an auxiliary code DOSE to calculate the dose rate after shutdown.

2.2.5 The ANDYKAY code

The ANDYKAY [41] code uses the adjoint method to construct linear decay chains. The code uses every possible radioisotope as the starting point of the linear decay chains. Then, isotopes which can transmute to the starting isotope are added to the chain. The code uses the following terminology:

- The radioisotope with which the linear decay chain begins is termed as the n'th isotope.
- The stable isotope with which the linear decay chain ends is termed as the first isotope.

The adjoint linear decay chain equations can be written as:

$$\frac{dN_i^*}{dt} - \beta_i N_i^* + \gamma_{i+1} N_{i+1}^* = 0 \qquad i = 1, 2, \ldots, n-1 \tag{2.25}$$

and

$$\frac{dN_n^*}{dt} - \beta_n N_n^* = 0 \tag{2.26}$$

where

N_i^* = the adjoint number density of the i'th nuclide ,

β_i = decay constant of nuclide i ,

γ_{i+1} = the production rate of nuclide $(i+1)$ from nuclide i.

The solution of equations (2.25) and (2.26) for a chain of length n if $N_n^*(t_f) \neq 0$ and $N_l^* = 0, \quad l = 1, 2, \ldots, n-1$ is:

$$N_m^*(\Delta t) = \prod_{k=m}^{n-1} \gamma_{k+1} \left[N_n^*(t_f) \sum_{j=n}^{m} \frac{e^{-\beta_j \Delta t}}{\prod_{i=n}^{m} (\beta_i - \beta j)} \right] \tag{2.27}$$

where $\Delta t = t_f - t$, and t_f is the final time.

For more than one non-zero $N^*(t_f)$, equation (2.27) will take the following form:

$$N_m^*(\Delta t) = \sum_{j=n}^{m} \prod_{k=m}^{j-1} \gamma_{k+1} \left[N_j^*(t_f) \sum_{l=m}^{j} \frac{e^{-\beta_j \Delta t}}{\prod_{i=m}^{j} (\beta_i - \beta_l)} \right] \tag{2.28}$$

Finally, an expression for the adjoint number density in terms of a series solution is:

$$N^*_{z+1}(t) \;=\; \sum_{j-1}^{z+1} a_j^{z+1}\, e^{\beta_j \Delta t} \tag{2.29}$$

where $z = n - k$.

The coefficients are generated by the use of the following recursion relations:

$$a_z^z \;=\; N^*_z(t_f) \;+\; \gamma_{z+1} \sum_{n}^{z+1} \frac{a_j^{z+1}}{\beta_j - \beta_z}, \tag{2.30}$$

and

$$a_j^z \;=\; \gamma_{z+1}\, \frac{a_j^{z+1}}{\beta_z - \beta_j}. \tag{2.31}$$

ACTLFIN is the cross section and decay data library that is used by the ANDYKAY code. This library is a combination of the ACTLPLUS library and cross sections from the DCDLIB. In turn, the ACTLPLUS library is a combination of the ACTL cross section data and the DCDLIB decay data libraries.

Chapter 3

Proton Activation Analysis

For years, activation analysis studies were conducted to investigate the effect of neutron-induced radioactivity on the process of selecting the different structural materials for fusion reactors. The appearance of D-^{3}He fusion reactors as a possible alternative to the D-D and D-T reactors brought up several questions not only about what level of radioactivity would be induced in such reactors due to proton interactions with the different structural materials, but also what kind of previously unconsidered radioisotopes may be produced and what sort of problems they would present as potential sources for radiological hazard for both the reactor safety and the long-term storage of fusion waste.

The two main sources of radioactivity production in D-^{3}He fusion reactors can be categorized as:

1. Proton-induced radioactivity, which in turn can be divided into the

radioactivities resulting from:

(a) The decay of the radioactive isotopes which are formed due to interactions of proton with the structural materials.

(b) Neutrons produced by proton interactions with the structural materials.

2. Neutron-induced radioactivity from both the D-D and D-T secondary reactions.

The development of protons and generally charged particles activation analysis has been slow due to the following reasons:

1. The detailed excitation functions for charged particle reactions are only known for very few elements and most of the time they are hard to find at the desired energy.

2. Charged particles have a limited penetration range in solids. There has been a general lack in the availability of reliable data for the range and the stopping power in all elements.

3. The probability of occurrence of several nuclear reactions simultaneously at the same charged particle energy increases the possibility of nuclear interference.

In this chapter an attempt will be made to answer the question regarding the level of radioactivity induced in D-^{3}He fusion reactors due to proton

interactions with the structural materials through the use of proton thick-target yields rather than nuclear cross sections.

3.1 Proton Thick-Target Yields

The main difficulty in the application of protons for activation analysis is the need to use nuclear cross sections. The nuclear cross section is not a convenient quantity to use for this purpose because it is strongly dependent on proton energy, such that it continually varies as protons slow down in the irradiated material. Figure (3.1) shows the general features of a proton excitation function [42].

The excitation function gradually increases from the reaction threshold energy and reaches a maximum as the proton energy approaches the target coulomb barrier energy. As shown in the Figure, the cross section for a particular nuclear reaction (σ_a) starts to decrease as the probabilities of occurrence of other nuclear reactions increase. However, the total cross-section (σ_t) for all possible nuclear reactions continues to increase as proton energy increases. One alternative quantity to cross section that is widely used is the thick-target yield Y, which is usually expressed in the units of μCi/μA.hr.

In the following subsection, the relation between a radioisotope activity and the thick-target yield will be developed.

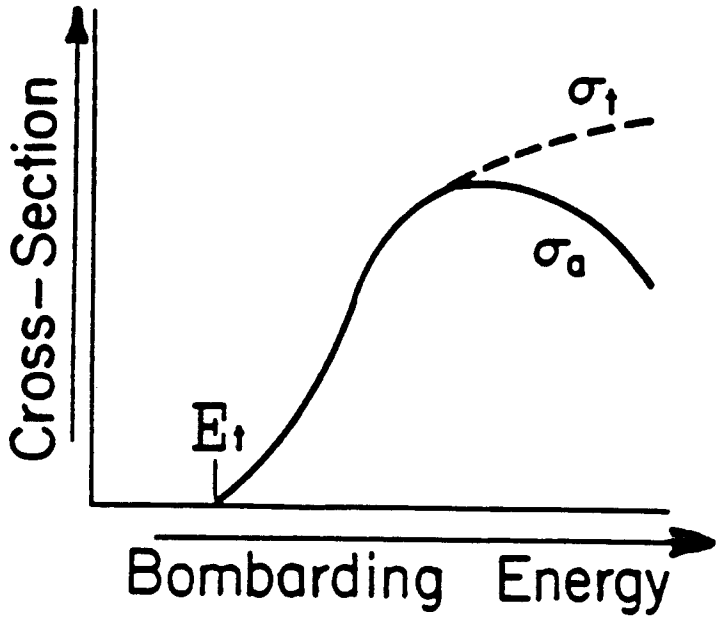

Figure 3.1: General features of proton excitation function.

3.1.1 Theory of Thick-Target Yield

The balance equation describing the formation and decay of a radioisotope during the irradiation of a thin target Δx [43] is:

$$\frac{dN}{dt} = \sigma n \phi \Delta x - \lambda N \tag{3.1}$$

where

N is the number of atoms of the radioisotope formed ,

σ (cm^2) is the parent atoms nuclear reaction cross section ,

n (atoms/gm) is the parent atoms concentration ,

ϕ (protons/s) is the proton flux ,

Δx (gm/cm^2) is the thickness of the thin target,

λ (s^{-1}) is the radioisotope decay constant ,

and

t (s) is the irradiation time.

In equation (3.1), the following three assumptions are made:

1. The parent atoms are stable, such that the radioactive isotopes are only produced as products of nuclear interactions between protons and the target material.

2. No chains are assumed (*i.e.*, no removal of the radioactive isotopes by absorption).

3. No regard to the reduction in the number of the parent atoms.

Integrating equation (3.1) yields:

$$N = \sigma n \phi \Delta x \left(\frac{1 - e^{-\lambda t}}{\lambda} \right) \tag{3.2}$$

Hence, the radioisotope activity in a thin target can be written as:

$$\Delta A = N\lambda = \sigma n \phi \Delta x \left(1 - e^{-\lambda t}\right) \tag{3.3}$$

The total radioisotope activity in a thick target can be found by integrating equation (3.3), yielding:

$$A = \left(1 - e^{-\lambda t}\right) n \int_0^{x_s} \sigma(x)\phi(x)dx \qquad \text{(dps)} \tag{3.4}$$

$x_s(\text{mg/cm}^2)$ is the proton range on the portion where $\sigma(x) \neq 0$, *i.e.*, on the portion where the proton energy is higher than the reaction threshold energy. The coordinate, $x = 0$, corresponds to the surface of a target in which the parent atom concentration is assumed to be uniform.

The proton flux varies significantly with target depth ($\phi = \phi(x)$) only for high proton energy ($\geq$ 100 MeV) [44] at which the total interactions cross section of protons with target nuclei greatly increase. But at energies 10 - 40 MeV, the loss of protons due to nuclear reactions is negligibly small. Therefore, the proton flux remains constant with target depth until they stop. *i.e.*, $\phi(x) = \phi_o$.

In such a case, equation (3.4) can be written as:

$$A = 2.703 \times 10^{-5}\, n\, \phi_o \left(1 - e^{-\lambda t}\right) \int_0^{x_s} \sigma(x)dx \qquad (\mu\text{Ci}) \tag{3.5}$$

Since most of cross sections are tabulated as function of energy, rearranging equation (3.5) yields:

$$A \;=\; 2.703 \times 10^{-5}\; n\; \phi_{\circ} \left(1 \;-\; e^{-\lambda t}\right) \int_0^{E_p} \frac{\sigma(E)}{S(E)}\; dE \qquad (3.6)$$

where

E_p (MeV) is the initial proton energy,

and

$S(E)(\mathrm{MeV} \cdot \mathrm{cm}^2/\mathrm{gm})$ is the stopping power of the parent atom.

Defining the proton flux in terms of a beam current $I(\mu\mathrm{A})$ and the relative proton charge Z $(Z = 1)$, one can write the flux in the form:

$$\phi \;=\; 6.25 \times 10^{12}\; \frac{I}{Z}$$

Substituting in equation (3.6), yields:

$$A \;=\; 1.69 \times 10^{8}\; n\; I\; \left(1 \;-\; e^{-\lambda t}\right) \int_0^{E_p} \frac{\sigma(E)}{S(E)}\; dE \qquad (3.7)$$

Finally the thick-target yield Y can be defined as:

$$Y \;=\; 1.69 \times 10^{8}\; n\; \lambda \int_0^{E_p} \frac{\sigma(E)}{S(E)}\; dE \qquad (\mu\mathrm{Ci}/\mu\mathrm{A.hr}) \qquad (3.8)$$

3.1.2 Development of a Proton-Induced Thick-Target Radionuclide Activation Yield Library

A computer program PTTY was developed to produce a proton thick-target yield library. Experimental cross section data were collected from several

publications [51,52,53]. Data for protons (with energy $\leq$ 14.7 MeV) interacting with 109 naturally occurring isotopes of 58 target elements were found. For most nuclear reactions several sets of data were found for the same reaction, but not all of the cross sections covered the same proton energy range. In many instances significant differences existed in the measured cross section values for the same proton energy. In the absence of enough information about the measuring techniques that would indicate the level of accuracy associated with most of the cross section data, an averaging technique was adopted such that all available data can be taken into consideration. Several nuclear reactions lead to the formation of two different radioactive isotopes through the formation of two isomeric states. For such reactions, where only the total cross section was given without having any other set of data for the same reaction that will help in estimating the branching ratio, a branching ratio of 50 % was assumed.

The proton stopping powers were taken from the most complete data sets compiled by Anderson and Zielger [54]. The authors used a mixture of experimentally and theoretically calculated proton stopping power values in compiling their report. At high proton energy ($\geq$ 1 MeV/amu), Anderson and Zielger calculated the stopping power by using the Bethe equation:

$$S = \frac{4\pi e^4 Z_1^2 Z_2}{mv^2} \left[\ln\left(\frac{2mv^2}{I_p}\right) + \ln\left(\frac{1}{1-\beta^2}\right) - \beta^2 - \frac{C}{Z_2} \right] \qquad (3.9)$$

Here, e and m are the electronic charge and mass, respectively, Z_1 and Z_2

are the proton and target material atomic numbers, respectively, v is the proton velocity, $\beta = v/c$, where c is the speed of light, I_p is the effective ionization potential and C/Z_2 is the shell correction factor. The shell correction factor for all available experimental data for the proton stopping power was calculated by substituting for the theoretical value of the effective ionization potential in the Bethe equation. Several smooth curves of C/Z_2 as a function of E (energy expressed in keV/amu) were drawn for several elements. For those elements where C/Z_2 values were not smoothly varying as a function of Z_2, the authors altered the shape of some shell correction factor curves by using a power series formula that best fit the particular curve.

The proton stopping data were used with the measured cross sections to calculate the thick-target activation yields for 164 radionuclides. Thick-target radionuclide yields as a result of (p,n), (p,γ), (p,α), (p,2n) and (p,pn) reactions are shown in Tables ((3.1), (3.2), (3.3), (3.4) and (3.5)), respectively. E_{min} and E_{max} are the minimum and maximum energies (in MeV) for which the cross section data were found in the literature.

Table 3.1: Thick-target yields of radionuclides produced by p,n reactions.

Target	E_{min}	E_{max}	Product	Y(μCi/μA.hr)
Li 7	1.88	5.50	Be 7	1.151E+02
Be 9	2.33	5.42	B 9	4.165E+26
B 10	4.94	11.70	C 10	3.710E+05
B 11	2.30	14.70	C 11	7.143E+05
C 13	3.24	5.27	N 13	5.268E+04
N 14	6.32	11.00	O 14	2.167E+06
N 15	3.72	14.70	O 15	3.124E+09
O 18	2.30	14.70	F 18	1.035E+05
F 19	4.21	4.93	Ne 19	2.264E+05
Na 23	4.85	11.60	Mg 23	1.092E+07
Mg 25	5.28	8.89	Al 25	1.348E+07
Mg 26	4.97	6.97	Al 26	1.338E-06
Mg 26	4.97	5.82	Al 26m	8.706E+05
Al 27	5.77	14.70	Si 27	5.258E+07
S 34	0.10	14.70	Cl 34m	8.315E+04
Cl 37	1.60	5.00	Ar 37	1.068E+01
K 41	1.11	5.96	Ca 41	1.408E-05
Sc 45	3.28	14.70	Ti 45	4.923E+04
Ti 47	4.00	14.00	V 47	2.142E+05
Ti 48	5.00	14.70	V 48	5.453E+02
Ti 49	1.30	6.00	V 49	3.075E+00
V 51	1.57	14.70	Cr 51	4.233E+02
Cr 52	5.80	14.70	Mn 52	4.541E+02
Cr 52	5.80	14.70	Mn 52m	3.153E+05
Cr 53	1.42	5.88	Mn 53	4.509E-07
Cr 54	2.22	9.00	Mn 54	1.175E+01
Mn 55	1.00	8.10	Fe 55	2.230E+00
Fe 56	4.80	14.70	Co 56	6.802E+01
Fe 57	1.60	14.00	Co 57	1.840E+01
Co 59	1.89	14.70	Ni 59	3.007E-04
Ni 60	6.70	14.70	Cu 60	2.441E+05
Ni 61	2.49	14.10	Cu 61	4.825E+04
Ni 62	4.82	14.70	Cu 62	1.023E+06
Ni 64	2.50	14.70	Cu 64	1.664E+04
Cu 63	3.80	14.70	Zn 63	2.478E+05
Cu 65	1.80	14.70	Zn 65	3.408E+01

Table 3.1. (continued)

Target	E_{min}	E_{max}	Product	Y(μCi/μA.hr)
Zn 64	8.10	11.90	Ga 64	6.993E+05
Zn 66	5.50	14.70	Ga 66	1.878E+04
Zn 67	1.85	6.37	Ga 67	1.948E+02
Zn 68	3.38	14.70	Ga 68	2.060E+05
Ga 69	3.00	14.70	Ge 69	6.579E+03
Ga 71	1.04	14.70	Ge 71	3.866E+02
Ga 71	1.04	14.70	Ge 71m	1.971E+10
Ge 74	3.42	5.83	As 74	1.025E+01
As 75	1.67	8.10	Se 75	1.131E+01
Se 77	2.18	14.70	Br 77	1.469E+03
Se 77	2.18	5.54	Br 77m	4.517E+04
Se 78	4.53	6.28	Br 78	5.477E+04
Se 80	2.67	6.39	Br 80	2.658E+04
Se 80	2.69	6.38	Br 80m	5.311E+02
Se 82	0.93	6.40	Br 82	3.394E+02
Br 79	3.00	14.70	Kr 79	4.965E+03
Rb 87	2.65	12.00	Sr 87m	1.645E+04
Sr 87	2.61	6.82	Y 87	1.064E+02
Sr 87	2.61	6.82	Y 87m	6.573E+02
Sr 88	4.80	14.70	Y 88	1.747E+03
Sr 88	4.80	14.70	Y 88m	3.864E+11
Y 89	3.55	14.70	Zr 89	1.369E+03
Y 89	3.66	14.70	Zr 89m	9.060E+05
Zr 90	7.00	14.70	Nb 90	3.560E+03
Zr 90	4.94	14.70	Nb 90m	1.266E+07
Zr 91	3.50	11.20	Nb 91m	3.883E+01
Zr 92	3.50	6.67	Nb 92	1.527E-09
Zr 92	3.50	9.00	Nb 92m	1.198E+02
Zr 96	2.73	9.00	Nb 96	1.767E+03
Nb 93	1.26	14.70	Mo 93	4.897E-03
Nb 93	1.26	14.70	Mo 93m	1.056E+03
Mo 94	6.00	9.00	Tc 94	4.457E+02
Mo 94	5.50	9.00	Tc 94m	2.129E+04
Mo 95	4.00	9.00	Tc 95	9.346E+02
Mo 95	4.00	9.00	Tc 95m	4.969E+00
Mo 96	10.00	14.70	Tc 96	6.866E+01

Table 3.1. (continued)

Target	E_{min}	E_{max}	Product	Y(μCi/μA.hr)
Mo 96	4.50	14.70	Tc 96m	1.452E+05
Mo 100	4.00	9.00	Tc 100	7.893E+06
Ru 100	4.25	6.19	Th 100	6.511E+01
Ru 100	4.25	6.19	Rh100m	1.745E+04
Ru 101	2.92	12.00	Rh101m	4.619E+02
Rh 103	2.31	10.00	Pd 103	1.046E+02
Pd 104	6.00	9.00	Ag 104	1.685E+03
Pd 104	6.00	9.00	Ag104m	3.912E+04
Pd 105	5.00	9.00	Ag 105	1.859E+01
Pd 105	4.00	9.00	Ag105m	5.588E+04
Pd 106	6.50	9.00	Ag 106	3.006E+04
Pd 106	6.00	9.00	Ag106m	1.103E+01
Pd 108	4.00	9.00	Ag 108	5.646E+05
Pd 110	2.11	9.00	Ag 110	3.374E+06
Pd 110	2.11	9.00	Ag110m	4.879E-01
Ag 107	1.90	14.70	Cd 107	1.853E+04
Ag 109	2.09	10.50	Cd 109	2.868E+00
Cd 110	4.50	14.70	In 110	9.810E+04
Cd 110	4.50	14.70	In110m	5.974E+03
Cd 111	1.50	14.70	In 111	1.090E+03
Cd 111	1.50	14.70	In111m	4.626E+05
Cd 112	3.14	14.70	In 112	3.183E+05
Cd 112	3.14	14.70	In112m	2.025E+05
Cd 113	4.70	14.70	In113m	1.648E+04
Cd 114	2.20	10.00	In 114	9.881E+05
Cd 114	2.20	14.70	In114m	3.986E+01
Cd 116	1.50	8.41	In 116	3.290E+06
Cd 116	1.50	14.70	In116m	2.188E+04
Sn 117	2.83	7.07	Sb 117	1.179E+03
Sn 118	4.53	6.92	Sb 118	4.691E+04
Sn 118	4.53	6.92	Sb118m	5.473E+02
Sn 119	2.62	7.08	Sb 119	9.395E+01
Sn 120	3.56	6.97	Sb 120	7.924E+03
Sn 120	3.68	6.97	Sb120m	1.158E+01
Sn 122	2.64	9.10	Sb 122	3.857E+02
Sn 122	2.64	9.10	Sb122m	5.858E+04

Table 3.1. (continued)

Target	E_{min}	E_{max}	Product	Y(μCi/μA.hr)
Sn 124	2.61	7.11	Sb 124	2.732E+00
Sb 121	5.20	9.00	Te 121	2.192E+01
Sb 121	5.20	9.00	Te121m	1.350E+00
Te 124	9.58	14.70	I 124	5.343E+02
Te 128	3.31	6.24	I 128	1.636E+03
Te 130	2.73	14.70	I 130	2.805E+03
Te 130	2.73	5.66	I 130m	9.982E+02
I 127	3.01	14.70	Xe 127	5.618E+01
I 127	3.01	14.70	Xe127m	2.454E+06
Ba 134	10.50	11.70	La 134	6.819E+03
La 139	4.50	10.30	Ce 139	3.836E+00
La 139	4.50	10.30	Ce139m	8.142E+05
Ce 142	3.80	14.70	Pr 142	7.114E+02
Ce 142	3.80	14.70	Pr142m	5.593E+04
Pr 141	4.84	14.70	Nd 141	3.622E+04
Pr 141	5.32	14.70	Nd141m	1.912E+06
Nd 148	9.00	14.70	Pm 148	4.318E+01
Nd 148	9.00	14.70	Pm148m	3.138E+00
Gd 160	4.30	14.70	Tb 160	5.873E+00
Tm 169	3.30	14.70	Yb 169	3.189E+01
Tm 169	3.30	14.70	Yb169m	1.916E+06
Hf 180	6.50	9.00	Ta180m	2.202E+02
Ta 181	4.50	14.70	W 181	3.655E+00
Au 197	7.00	14.70	Hg 197	9.733E+01
Au 197	7.00	14.70	Hg197m	2.632E+02
Pb 206	5.00	14.70	Bi 206	2.030E+02
Bi 209	2.90	14.70	Po 209	1.906E-02

Table 3.2: Thick-target yields of radionuclides produced by p,γ reactions.

Target	E_{min}	E_{max}	Product	Y(μCi/μA.hr)
C 12	0.09	11.00	N 13	9.179E+03
Ca 42	0.69	5.43	Sc 43	8.665E+00
Ni 60	0.61	14.70	Cu 61	2.004E+02
Zn 64	1.47	11.00	Ga 65	1.151E+03
Se 82	6.85	14.70	Br 83	1.006E+02
Zr 90	1.97	5.70	Nb 91	1.262E-06
Zr 90	1.97	5.70	Nb 91m	7.434E-02
Mo 100	8.00	14.70	Tc 101	7.207E+02
Cd 114	3.00	8.00	In115m	4.906E+00
Sn 112	5.00	9.00	Sb 113	1.802E+04
Te 130	6.00	14.70	I 131	7.418E-01
Ce 142	5.50	14.70	Pr 143	2.778E-01
Bi 209	6.00	14.70	Po 210	2.292E-02

Table 3.3: Thick-target yields of radionuclides produced by p,α reactions.

Target	E_{min}	E_{max}	Product	Y(μCi/μA.hr)
N 14	4.00	14.70	C 11	4.807E+05
O 16	6.22	14.70	N 13	1.664E+05
Ne 20	5.58	10.28	F 17	1.667E+06
Mg 24	9.22	13.75	Na 21	2.863E+06
Mg 25	5.00	14.70	Na 22	2.904E+00
Ni 58	7.40	14.70	Co 55	3.032E+02
Ni 60	6.80	14.70	Co 57	2.054E+00
Ni 61	7.00	14.40	Co 58	9.220E+00
Ni 61	7.00	14.40	Co 58m	1.722E+03
Zn 64	7.10	14.70	Cu 61	4.404E+03
Zr 90	12.00	14.70	Y 87	2.737E+00
Zr 90	12.00	14.70	Y 87m	1.691E+01
Sn 120	3.50	14.70	In117m	1.634E+01
Hg 202	12.00	14.70	Au 199	4.723E-02

Table 3.4: Thick-target yields of radionuclides produced by p,2n reactions.

Target	E_{min}	E_{max}	Product	Y(μCi/μA.hr)
Cu 63	14.00	14.70	Zn 62	9.859E+00
Ga 69	13.10	14.70	Ge 68	3.278E+00
Y 89	13.30	14.70	Zr 88	1.617E+00
Cd 110	12.60	14.70	In 109	1.698E+03
Cd 110	12.80	14.70	In109m	6.538E+04
Cd 111	11.80	14.70	In 110	2.130E+04
Cd 111	11.20	14.70	In110m	8.493E+02
Cd 112	9.40	14.70	In 111	5.071E+02
Cd 112	10.80	14.70	In111m	9.079E+04
Te 124	12.20	14.70	I 123	9.103E+02
Pr 141	9.00	14.70	Nd 140	4.863E+02

Table 3.5: Thick-target yields of radionuclides produced by p,pn reactions.

Target	E_{min}	E_{max}	Product	Y(μCi/μA.hr)
C 12	8.50	14.70	C 11	1.285E+04
Sc 45	11.30	14.70	Sc 44	2.467E+03
Sc 45	12.00	14.70	Sc 44m	1.029E+02
Co 59	12.00	14.70	Co 58	4.450E-01
Co 59	12.10	14.70	Co 58m	1.464E+02
Cu 63	14.00	14.70	Cu 62	5.984E+03
Cu 65	9.80	14.70	Cu 64	3.105E+02
Ga 69	13.90	14.70	Ga 68	2.094E+03
Br 81	10.00	14.70	Br 80	6.457E+03
Br 81	0.15	14.70	Br 80m	1.128E+03
Y 89	12.70	14.70	Y 88	7.672E-01
Y 89	12.70	14.70	Y 88m	9.814E+08
Ag 107	8.78	14.70	Ag 106	1.356E+03
Ag 107	11.00	14.70	Ag106m	8.894E+00
Cd 110	12.60	14.70	Cd 109	7.318E-02
Ta 181	13.40	14.70	Ta180m	4.874E+00
Au 197	10.00	14.70	Au 196	1.464E+00
Au 197	10.00	14.70	Au196m	2.235E+01

3.2 Activity Calculation

Another computer program PIAC was written to calculate proton-induced activity by using the proton thick-target yield library. The equations used in the program are defined as follows:

From equations (3.7) and (3.8), the final definition of a radioisotope activity in terms of thick-target yield takes the form:

$$A = YI\left(\frac{1 - e^{-\lambda t}}{\lambda}\right) \qquad (\mu\text{Ci}) \qquad (3.10)$$

If the parent element i is contained as a homogeneous admixture in an irradiated material m, then the activity of the resulting radioisotope k can be found from the relation [45] :

$$^{k}A_{im} = Y_{im}\, I\left(\frac{1 - e^{-\lambda_k t}}{\lambda_k}\right) \qquad (3.11)$$

with

$$Y_{im} = Y\, \eta_{im}\, F \qquad (3.12)$$

where

Y is the thick-target yield of the radioisotope k for a thick target consisting entirely of the element i ,

η_{im} is the relative concentration (by weight) of the element i in the material m ,

and

F is a factor which takes into account the difference of the stopping powers of the parent element i and of the irradiated alloy or chemical compound m.

The factor F can be obtained by one of the following three equations ((3.13), (3.14) and (3.15)): [45,46,47,48]

The first equation is:

$$F = \frac{R_m}{R_i} = \frac{1}{x_1 + x_2\frac{R_1}{R_2} + x_3\frac{R_1}{R_3} + \cdots} \tag{3.13}$$

where

R_i is the range of the proton in the parent element i ,

R_m is the range of the proton in the irradiated material m ,

$R_1, R_2, R_3, \cdots$ are the ranges of the proton in the individual elements forming the irradiated material m ,

and

$x_1, x_2, x_3, \cdots$ are the weight proportions of the individual elements in the target compound.

The second equation is:

$$F = \frac{P_m}{P_i} = \frac{1}{x_1 + x_2\frac{P_1}{P_2} + x_3\frac{P_1}{P_3} + \cdots} \tag{3.14}$$

where the range R in equation (3.13) is replaced by a proportional coefficient P.

Since one approximation to the range/energy relation is that range $\propto E^{1.75}$ [49], the physical meaning of the coefficient P can be deduced from the following relation: [47] [50]

$$R = \frac{A}{Z_A} I_A^{1/4} \left(\frac{2.4E^{1.75}}{Z_a^2 a^{3/4}} \right) = P \left(\frac{2.4E^{1.75}}{Z_a^2 a^{3/4}} \right)$$

This implies that:

$$P = \frac{A}{Z_A} I_A^{1/4}$$

Here, R denotes the range (mg/cm^2), I_A is the effective ionization potential of the irradiated material (keV), A and a are the mass numbers of the irradiated element and the proton, respectively, Z_A and Z_a denotes the relative charge of the target nuclei and the impinging proton, respectively and E is the proton energy (MeV). Some of the P coefficients are listed in Table (3.6) [47].

The third equation is:

$$F = \frac{F(\langle E_p \rangle, Z_m)}{F(\langle E_p \rangle, Z_p)} \tag{3.15}$$

where

$F(\langle E_p \rangle, Z)$ = correction factor for a target consists mainly of an element with proton number Z. Values for proton projectiles are shown in Figure (3.2) [48] ,

$\langle E_p \rangle$ = mean projectile energy. Defined as weighted average using the activity produced in small energy intervals as weight factors.

Element	P value	Element	P value
H	0.364	Tc	1.892
He	0.833	Ru	1.898
Li	1.066	Rb	1.899
Be	1.115	Pd	1.930
B	1.120	Ag	1.925
C	1.078	Cd	1.970
N	1.114	In	1.985
O	1.147	Sn	2.020
F	1.243	Sb	2.041
Ne	1.214	Te	2.106
Na	1.281	I	2.065
Mg	1.265	Xe	2.105
Al	1.324	Cs	2.102
Si	1.298	Ba	2.141
P	1.353	La	2.136
S	1.330	Ce	2.126
Cl	1.402	Pr	2.111
Ar	1.509	Nd	2.132
K	1.414	Pm	2.117
Ca	1.391	Sm	2.167
Sc	1.502	Eu	2.163
Ti	1.541	Gd	2.211
V	1.583	Tb	2.209
Cr	1.562	Dy	2.223
Mn	1.599	Ho	2.240
Fe	1.576	Er	2.245
Co	1.615	Tu	2.243
Ni	1.565	Yb	2.272
Cu	1.648	Lu	2.273
Zn	1.650	Hf	2.293
Ga	1.716	Ta	2.300
Ge	1.743	W	2.313
As	1.758	Re	2.318
Se	1.809	Os	2.344
Br	1.790	Ir	2.345
Kr	1.837	Pt	2.357
Rb	1.835	Au	2.356
Sr	1.843	Hg	2.377
Y	1.832	Tl	2.399
Zr	1.844	Pb	2.409
Nb	1.842	Bi	2.408
Mo	1.868	Po	2.398

Table 3.6: Coefficients P for Various Elements.

as

$$\langle E_p \rangle \simeq \begin{cases} E_{max} & \text{if} \quad E_p \geq E_{max} \\ E_p - 1\text{MeV} & \text{if} \quad E_p < E_{max} \end{cases}$$

Here

E_{max} = the maximum energy in the projectile (proton) energy spectrum ,

Z_p = proton number of the projectile ,

Z_m = weighted average of the proton number of the target material $= \sum C_x Z_x$,

C_x = concentration by weight of the element with the proton number Z_x in the target material.

Since the values of the factor F obtained by the previous three equations are very similar, the second equation (using the P coefficients from Table (3.6)) has been used in the proton activation calculations in the next chapter.

Finally, if a radioisotope k is formed simultaneously from several elements in the target. The radioisotope activity can be written as:

$$^{k}A_m = I \left(\frac{1 - e^{-\lambda_k t}}{\lambda_k} \right) \sum_j Y_{jm} \qquad (3.16)$$

The index j refers to an element in the target material that will produce the radioactive isotope through a nuclear reaction with the incident proton.

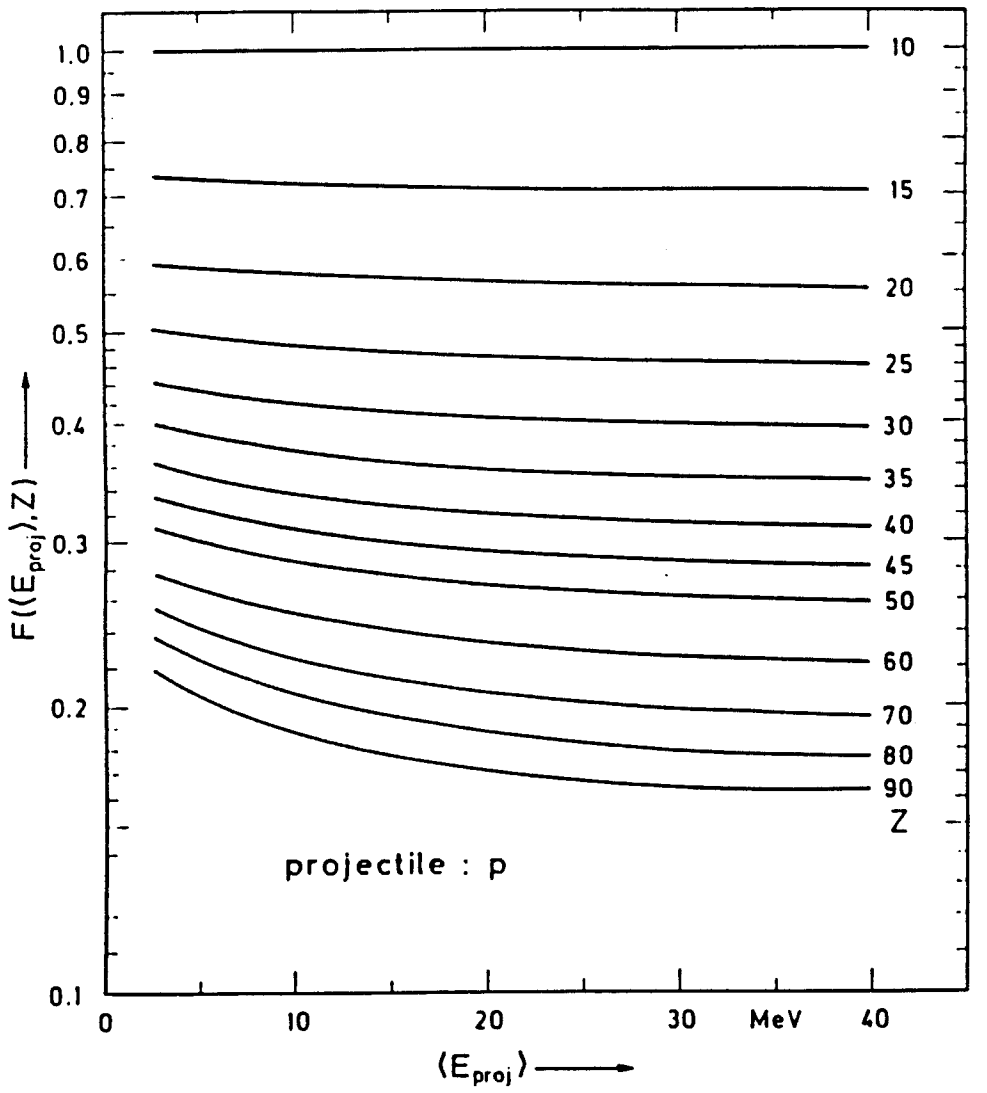

Figure 3.2: Dependence of the correction factor $F(\langle E_{proj}\rangle, Z)$ on the mean projectile energy $\langle E_{proj}\rangle$ and the proton number Z of the target material for reactions with protons.

Chapter 4

Neutron Energy Spectrum

4.1 Introduction

The neutron-induced radioactivity in D-^{3}He fusion reactors is mainly dominated by neutrons produced from the D-D and D-T secondary reactions. The energies of such neutrons are quite high being approximately 2.45 and 14.1 MeV, and nearly monoenergetic for D-D and D-T secondary reactions, respectively. Another source of neutrons that needs to be considered is the neutrons produced by the proton interactions with the different structural materials in the reactor. Although contributions from such neutrons to the total level of radioactivity in D-^{3}He fusion reactors is expected to be minimal, an evaluation of their effect is needed to have a comprehensive analysis of the radioactivity induced in D-^{3}He fusion reactors.

Previous studies did examine the question of evaluating the energy spec-

trum of neutrons produced from both the D-D and D-T secondary reactions. In this chapter, an attempt is made to obtain an approximate evaluation for the energy spectrum of the remaining source of neutrons (produced from proton interactions with the reactor structure through (p,n) reactions) by using the multigroup transfer matrices method.

4.2 Multigroup Transfer Matrices Method

This multigroup transfer matrices method has been developed by Perkins [56,57] of Lawerence Livermore National Laboratory. A review of the method is presented in this section. Although very good results can be obtained by using this method, a major shortcoming is the need to have experimentally measured angular distributions of the neutrons produced for all elements in the reactor structure. Such angular distribution data are only available so far for few light elements. It is important to emphasize here that in the absence of available data for most heavy elements, an isotropic center of mass angular distribution has been considered in this thesis.

4.2.1 The General Two-Body Interaction

In the discrete two-body reaction, the projectile "1" of mass M_1, velocity V_1, momentum P_1 and energy E_1, interacts with a stationary target "2" of mass M_2 yielding reaction products $x(M_x, V_x, P_x, E_x)$ and $y(M_y, V_y, P_y, E_y)$ (Fig.

(4.1)).

The method used to describe such an interaction is based on two basic assumptions:

1. The reaction is nonrelativistic as the projectile kinetic energy is much less than its rest mass energy.

2. The target is considered to be at rest as its thermal motion is negligible compared to the kinetic energy of the projectile.

Conservation of momentum and energy in the laboratory system yields: [55, 56]

$$\vec{P}_1 = \vec{P}_x + \vec{P}_y \tag{4.1}$$

and

$$E_1 + Q = E_x + E_y \tag{4.2}$$

where Q is the reaction Q-value, and can be written as:

$$Q = Q_o + (W_1 + W_2 - W_x - W_y)$$

and

$$Q_o = (M_1 + M_2 - M_x - M_y)\, C^2$$

where W refers to level excitation energy. Equation (4.1) and Figure (4.2) give:

$$P_y^2 = P_1^2 + P_x^2 - 2P_1 P_x \cos\vartheta \tag{4.3}$$

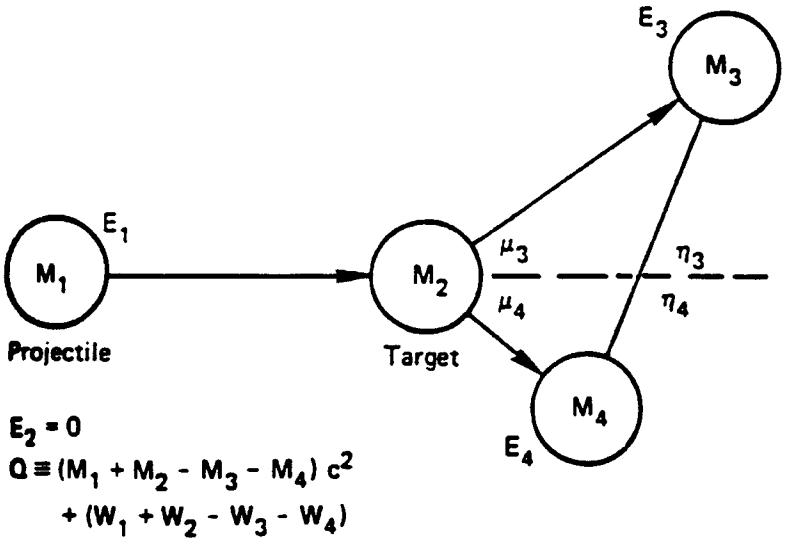

Figure 4.1: Nomenclature for two-body reaction. The η 's are the collision cosines in the center of mass system and the μ 's are the corresponding cosines in the laboratory system.

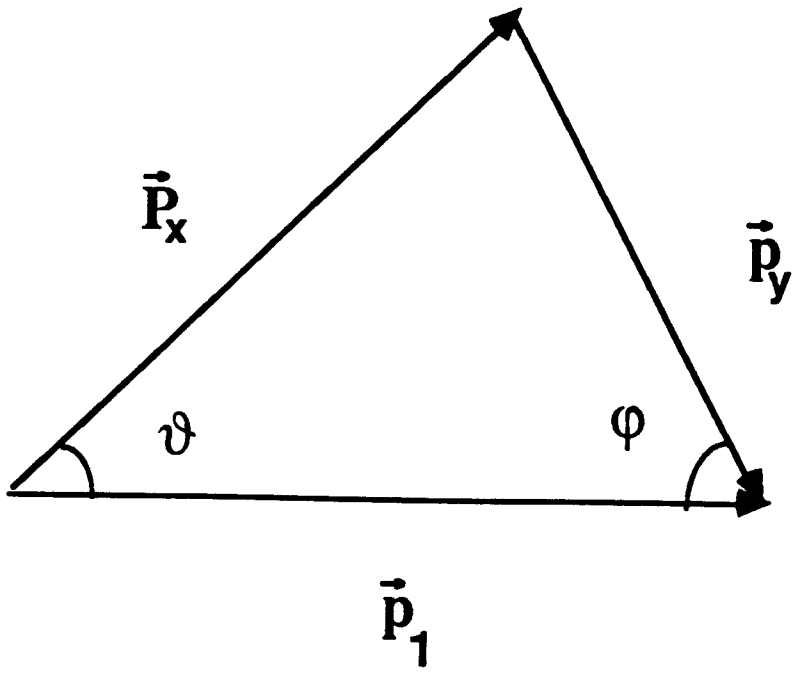

Figure 4.2: Momentum conservation. ϑ and φ are the angles of emission of the two products x and y respectively.

Expressing the momenta in terms of the corresponding kinetic energies allows the elimination of E_y from equation (4.2) and yields:

$$Q = \frac{M_x + M_y}{M_y} E_x - \frac{M_y - M_1}{M_y} E_1 - 2\frac{\sqrt{M_1 M_x}}{M_y}\sqrt{E_1}\sqrt{E_x}\cos\vartheta \quad (4.4)$$

Solving equation (4.4) with respect to E_x, one gets:

$$E_x = \left[\frac{\sqrt{M_1 M_x}}{(M_x + M_y)^2}\sqrt{E_1}\cos\vartheta \pm \sqrt{\left[\frac{M_y - M_1}{(M_x + M_y)} + \frac{M_1 M_x}{(M_x + M_y)^2}\cos^2\vartheta\right] E_1 + \frac{M_y}{(M_x + M_y)} Q}\right]^2 \quad (4.5)$$

The energy E_x may be expressed in terms of its center of mass collision cosine η_x as: [56,57]

$$E_x = a_{1x}E_1 + a_{2y}(E_1 - E_{1\alpha}) + 2\left[a_{1x}a_{2y}E_1(E_1 - E_{1\alpha})\right]^{1/2}\eta_x \quad (4.6)$$

where

$$a_{1x} = \frac{M_1 M_x}{(M_1 + M_2)(M_x + M_y)},$$

$$a_{2y} = \frac{M_2 M_y}{(M_1 + M_2)(M_x + M_y)},$$

$$E_{1\alpha} = -\left(\frac{M_1 + M_2}{M_2}\right) Q.$$

$E_{1\alpha}$ is the reaction threshold energy.

Since all collision angles are possible in the center of mass system, the maximum and minimum values of E_x occur when $\eta_x = +1$ or -1, respectively.

These bounds are given by:

$$\underset{min}{E_{x_{max}}}(E_1) = a_{1x}E_1 + a_{2y}(E_1 - E_{1\alpha}) \pm 2\left[a_{1x}a_{2y}E_1(E_1 - E_{1\alpha})\right]^{1/2} \quad (4.7)$$

Inverting equation (4.7), the corresponding projectile energy, $\underset{min}{E_1}(E_{x_{max}})$ is found to be:

$$\underset{min}{E_1}(E_{max}) = \frac{-b \pm (b^2 - 4ac)^{1/2}}{2a} \quad (4.8)$$

where

$$a = -(a_{1x} - a_{2y})^2 ,$$

$$b = 2(\underset{min}{E_{x_{max}}} + a_{2y}E_{1\alpha})(a_{1x} + a_{2y}) - 4a_{1x}a_{2y}E_{1\alpha} ,$$

$$c = -(\underset{min}{E_{x_{max}}} + a_{2y}E_{1\alpha})^2 .$$

In the laboratory system, not all collision cosines are possible. Expressing equation (4.5) in terms of the laboratory collision cosine μ_x yields: [56]

$$E_x = a_{1x}E_1 \left\{ \mu_x \pm \left[\frac{a_{2y}}{a_{1x}} \frac{(E_1 - E_{1\alpha})}{E_1} - 1 + \mu_x^2 \right]^{1/2} \right\}^2 \quad (4.9)$$

The plus sign in equation (4.9) is to be used unless, $a_{1x}E_1 \geq a_{2y}(E_1 - E_{1\alpha})$.

4.2.2 The Angular Domain

Both the center of mass collision cosines η_x and the laboratory collision cosine μ_x can be obtained in terms of the particle energy from equations (4.6) and (4.9), respectively as:

$$\eta_x(E_1, E_x) = \frac{E_x - a_{1x}E_1 - a_{2y}(E_1 - E_{1\alpha})}{2\left[a_{1x}a_{2y}E_1(E_1 - E_{1\alpha})\right]^{1/2}} \quad (4.10)$$

and

$$\mu_x(E_1, E_x) = \frac{1}{2\ (a_{1x}E_1E_x)^{1/2}}\ [a_{1x}E_1 - a_{2y}(E_1 - E_{1\alpha}) + E_x] \qquad (4.11)$$

In equation (4.11) [56], $\mu_x = 0$ if $E_x = 0$.

4.2.3 Reduction of the Transference Function

The transference function $\sigma(E_1 \rightarrow E_x, \mathbf{\Omega_1} \rightarrow \mathbf{\Omega_x})$ is defined as the cross section for a projectile of energy E_1 travelling in the direction $\mathbf{\Omega_1}$ to undergo a nuclear reaction releasing reaction product x into unit energy at E_x and into unit solid angle at $\mathbf{\Omega_x}$. Expressing the transference function as a function of a Legendre polynomial expansion in terms of the laboratory system collision cosines results in:

$$\sigma(E_1 \rightarrow E_x, \mathbf{\Omega_1} \rightarrow \mathbf{\Omega_x}) \ = \ \sum_{l=0}^{\infty} \frac{2l+1}{4\pi}\ \sigma_l(E_1 \rightarrow E_x)\ P_l(\mu_x)$$

where

$$\sigma_l(E_1 \rightarrow E_x) \ = \ 2\pi \int_{-1}^{+1} \sigma(E_1 \rightarrow E_x, \mathbf{\Omega_1} \rightarrow \mathbf{\Omega_x})\ P_l(\mu_x)\ d\mu_x$$

This leads to the final expression for $\sigma_l(E_1 \rightarrow E_x)$ being written as:

$$\sigma_l(E_1 \rightarrow E_x) \ = \ \sigma(E_1)\ \frac{d}{dE_x}\eta_x(E_1, E_x)\ P_l[\mu_x(E_1, E_x)]\ g[E_1, \eta_x(E_1, E_x)] \qquad (4.12)$$

where from equation (4.10), one obtains:

$$\frac{d}{dE_x}\eta_x(E_1, E_x) \ = \ \frac{1}{2\ [a_{1x}a_{2y}E_1(E_1 - E_{1\alpha})]^{1/2}} \qquad (4.13)$$

and $g[E_1, \eta_x(E_1, E_x)]$ being a unit normalized center of mass angular distribution over $-1 \leq \eta_x \leq +1$.

4.2.4 Derivation of the Multigroup Transfer Matrices

Consider a projectile within dE_1 at E_1 and in group g, $E_{g-1} \leq E_1 \leq E_g$, undergoing a nuclear reaction releasing a reaction product x within dE_x at E_x and in group j, $E_{j-1} \leq E_x \leq E_j$. The l' th component of the multigroup transfer cross section may be written in terms of the projectile flux $\phi_l(E_1)$ as:

$$\sigma_{l_{g\to j}} = \frac{\int_{E_1^-}^{E_1^+} dE_1 \phi_l(E_1) \int_{E_x^-(E_1)}^{E_x^+(E_1)} \sigma_l(E_1 \to E_x) dE_x}{\int_{E_{g-1}}^{E_g} \phi_l(E_1) dE_1} \tag{4.14}$$

where the integration limits in equation (4.14) are:

$$E_1^- = \max \left[E_{g-1};\ E_{1\alpha};\right.$$
$$\left. \begin{array}{ll} E_1(E_{x_{max}} = E_{j-1}) & \text{if } E_{x_{min}}(E_{1\alpha}) \leq E_{j-1} \\ E_1^-(E_{x_{min}} = E_j) & \text{if } E_j \leq E_{x_{min}}(E_{1\alpha}) \end{array} \right],$$

$$E_1^+ = \min \left[E_j;\ E_1^+(E_{x_{min}} = E_j) \right],$$

$$E_x^-(E_1) = \max \left[E_{j-1};\ E_{x_{min}}(E_1) \right],$$

$$E_x^+(E_1) = \min \left[E_j;\ E_{x_{max}}(E_1) \right].$$

with

$E_1^-(E_{x_{min}})$ uses the minus sign in equation (4.8),

and

$E_1^+(E_{x_{min}})$ uses the plus sign in equation (4.8).

Equation (4.14) can be rewritten as:

$$\sigma_{l_{g\to j}} = \frac{\int_{E_1^-}^{E_1^+} dE_1 \phi_l(E_1)\ Z_l(E_1)}{\int_{E_{g-1}}^{E_g} \phi_l(E_1) dE_1} \tag{4.15}$$

where

$$Z_l(E_1) \ = \ \int_{E_x^-(E_1)}^{E_x^+(E_1)} \sigma_l(E_1 \to E_x) dE_x \tag{4.16}$$

i.e.,

$$Z_l(E_1) = \sigma(E_1) \int_{E_x^-(E_1)}^{E_x^+(E_1)} \frac{d}{dE_x} \eta_x(E_1, E_x) P_l[\mu_x(E_1, E_x)] g[E_1, \eta_x(E_1, E_x)] dE_x \tag{4.17}$$

Equation (4.17) represents an integral over final particle energy E_x which can be done analytically as follows: [57]

Assuming that the center of mass angular distribution $g[E_1, \eta_x(E_1, E_x)]$ is piecewise linear in η_x [58] (as in Figure (4.3)), the angular bin i may be defined such that $\eta_{x_i} \ \leq \ \eta_x \ \leq \ \eta_{x_{i+1}}$. So, within this bin:

$$g[E_1, \eta_x(E_1, E_x)] \ = \ a_i \ + \ b_i \eta_x(E_1, E_x) \tag{4.18}$$

A definition of the angular domain that covers the energy limits imposed on

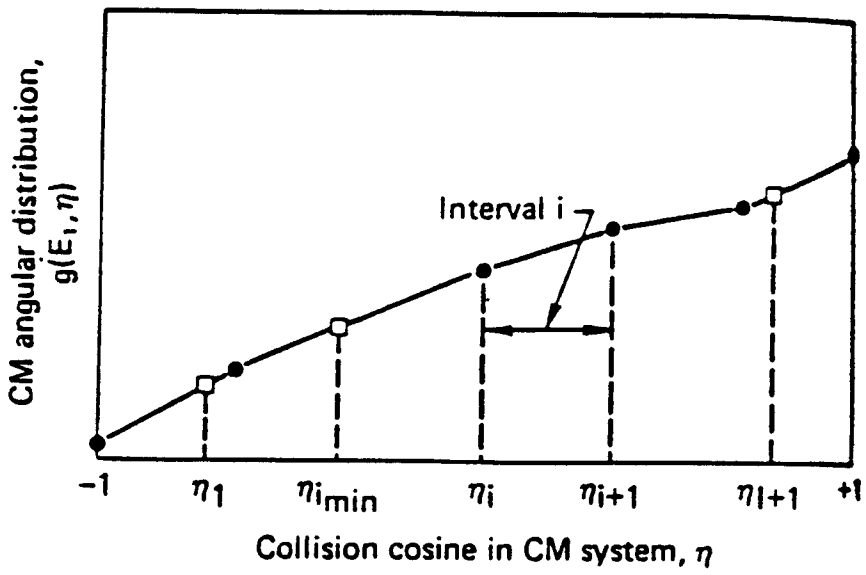

Figure 4.3: A piecewise linearly interpolable angular distribution. The solid points are the original data and the boxed points are linearly interpolable break points.

the integral in equation (4.17) takes the form:

$$\eta_1 = \eta[E_1, E_x^-(E_1)]$$

and

$$\eta_{I+1} = \eta[E_1, E_x^+(E_1)]$$

Expressing $Z_l(E_1)$ as a sum of integrals over energy ranges corresponding to the angular bins yields:

$$Z_l(E_1) = \sigma(E_1) \sum_{i=1}^{I} Z_{l_i}(E_1) \tag{4.19}$$

where

$$Z_{l_i}(E_1) = \int_{E_x(E_1,\eta_{x_i})}^{E_x(E_1,\eta_{x_{i+1}})} \frac{d}{dE_x}\eta_x(E_1, E_x)P_l[\mu_x(E_1, E_x)][a_i+b_i\eta_x(E_1, E_x)]dE_x \tag{4.20}$$

The next step is to change the variable of integration in equation (4.20) from the final particle energy E_x to its laboratory system collision cosine μ_x. The relationships between the center of mass and laboratory system collision cosines (η_x, μ_x) and the final particle energy E_x are:

$$\eta_x = \alpha(\mu_x \pm r)^2 - \gamma \tag{4.21}$$

and

$$\mu_x = \frac{\left(\frac{\eta_x}{2\alpha} + 1\right)}{\left(\frac{\eta_x + \gamma}{\alpha}\right)^{1/2}} \tag{4.22}$$

where

$$\alpha = \frac{a_{1x}E_1}{2\,[a_{1x}a_{2y}E_1(E_1 - E_{1\alpha})]^{1/2}} ,$$

$$r = (\beta^2 + \mu_x^2)^{1/2} ,$$

$$\beta^2 = \frac{a_{2y}}{a_{1x}} \frac{(E_1 - E_{1\alpha})}{E_1} - 1 ,$$

$$\gamma = \alpha\,(\beta^2 + 2) .$$

In equation (4.21) the positive sign is used for $\beta^2 \geq 0$ and the negative sign is used for $\beta^2 < 0$, for which the minimum possible laboratory system collision cosine can be written as:

$$\mu_{x_{min}} = (-\beta^2)^{1/2} \tag{4.23}$$

This implies that the positive sign is to be used in equation (4.21) for $E_x \geq E_x(\mu_{x_{min}})$ and the negative sign to be used for $E_x < E_x(\mu_{x_{min}})$ where:

$$E_x(\mu_{x_{min}}) = a_{1x}E_1 - a_{2y}(E_1 - E_{1\alpha})$$

The center of mass collision cosine μ_x corresponding to $\mu_{x_{min}}$ is:

$$\eta_x(\mu_{x_{min}}) = -(1 + \beta^2)^{1/2} \tag{4.24}$$

Differentiating equation (4.21) with respect to μ_x yields:

$$\frac{d\eta_x}{d\mu_x} = \pm \frac{2\alpha}{r} (\mu_x \pm r)^2 \tag{4.25}$$

Changing the variables of integration in equation (4.20) from E_x to μ_x yields:

$$Z_{l_i}(E_1) = \int_{\mu_x(E_1,\eta x_i)}^{\mu_x(E_1,\eta x_{i+1})} \frac{d}{dE_x}\eta_x(E_1,E_x)P_l[\mu_x(E_1,E_x)][a_i+b_i\eta_x(E_1,E_x)]d\mu_x \tag{4.26}$$

and the summation of equation (4.19) over the bins is:

$$Z_l(E_1) \;=\; \sigma(E_1)\left[\sum_{i=1}^{i_{min}-1} Z_{l_i}(E_1) \;+\; \sum_{i=i_{min}}^{I} Z_{l_i}(E_1)\right] \tag{4.27}$$

where i_{min} refers to $\eta_{x_i}(\mu_{x_{min}})$, which is the interpolated break point in the center of mass angular distribution corresponding to equation (4.24) if $\beta^2 \;<\; 0$.

So, for all bins less than i_{min}, the negative sign is used in equation (4.21), while the positive sign is used for all bins at or above i_{min}. If $\beta^2 \;\geq\; 0$, only the positive sign is used in equation (4.21), and equation (4.27) reduces to a single summation over $1 \;\leq\; i \;\leq\; I$.

Expressing $P_l[\mu_x(E_1,E_x)]$ in terms of a power series yields: [57,59]

$$P_l[\mu_x(E_1,E_x)] \;=\; \frac{1}{d_l}\sum_{m=0}^{l} C_{m,l}\;\mu_x^m(E_1,E_x) \tag{4.28}$$

where all values of $C_{m,l}/d_l$ can be obtained recursively from the relation:

$$\frac{1}{d_l}C_{m,l} \;=\; \frac{(2l\;-\;1)}{l}\;\frac{1}{d_{l-1}}\;C_{m-1,l-1} \;-\; \frac{(l\;-\;1)}{l}\;\frac{1}{d_{l-2}}\;C_{m,l-2}$$

for $0 \;\leq\; m \;\leq\; l$. $C_{m,l} = 0$ for $m < 0$ and $m > l$.

With the initial values $C_{0,0}/d_0 = C_{1,1}/d_1 = 1$ & $C_{0,1}/d_1 = 0$.

Substituting equations (4.21), (4.25) and (4.28) into equation (4.26), yields:

$$Z_{l_i} = (a_i - b_i\gamma)Z^{\circ}_{l_i}(E_1) + b_i Z^{1}_{l_i}(E_1) \tag{4.29}$$

where

$$Z^{\circ}_{l_i}(E_1) = \pm\frac{2\alpha}{d_l}\sum_{m=0}^{l} C_{m,l}\int_{\mu_{x_i}}^{\mu_{x_{i+1}}}\left(\frac{\mu_x^{m+2}}{r} \pm 2\mu_x^{m+1} + \mu_x^m r\right)d\mu_x \tag{4.30}$$

and

$$\begin{aligned} Z^{1}_{l_i}(E_1) = \pm\frac{2\alpha^2}{d_l}\sum_{m=0}^{l} C_{m,l}\int_{\mu_{x_i}}^{\mu_{x_{i+1}}}\Bigg(&\frac{\mu_x^{m+4}}{r} \pm 8\mu_x^{m+3} \\ &\pm 4\beta^2\mu_x^{m+1} + 6\mu_x^{m+2}r + \mu_x^m r^3\Bigg)d\mu_x \end{aligned} \tag{4.31}$$

Here

$$\mu_{x_i} = \mu_x(E_1, \eta_{x_i})$$

Integrating $Z^{\circ}_{l_i}(E_1)$ and $Z^{1}_{l_i}(E_1)$ analytically [57] gives:

$$Z^{\circ}_{l_i}(E_1) = \pm\frac{2\alpha}{d_l}\sum_{m=0}^{l} C_{m,l}\left[\kappa^{\circ}_m(\mu_{x_{i+1}}) - \kappa^{\circ}_m(\mu_{x_i})\right] \tag{4.32}$$

where

$$\kappa^{\circ}_m(\mu_{x_i}) = 2h_{m+2}(\mu_{x_i}) + \beta^2 h_m(\mu_{x_i}) \pm 2f_{m+1}(\mu_{x_i}) \tag{4.33}$$

and

$$Z^{1}_{l_i}(E_1) = \pm\frac{2\alpha^2}{d_l}\sum_{m=0}^{l} C_{m,l}\left[\kappa^{1}_m(\mu_{x_{i+1}}) - \kappa^{1}_m(\mu_{x_i})\right] \tag{4.34}$$

with

$$\kappa_m^1(\mu_{x_i}) = \left[1 + 3\left(\frac{2m+1}{m+1}\right)\right] h_{m+4}(\mu_{x_i}) + 3\left(\frac{2m+1}{m+1}\right)\beta^2 h_{m+2}(\mu_{x_i}) \pm 8 f_{m+3}(\mu_{x_i}) \pm 4\beta^2 f_{m+1}(\mu_{x_i}) + f_m(\mu_{x_i}) r^3 \quad (4.35)$$

In equations (4.33) and (4.35):

$$f_m(\mu_{x_i}) = \frac{\mu_{x_i}^{m+1}}{m+1} \quad (4.36)$$

and

$$h_m(\mu_{x_i}) = \frac{\mu_{x_i}^{m-1}}{m} r - \left(\frac{m-1}{m}\right)\beta^2 h_{m-2}(\mu_{x_i}) \quad (4.37)$$

where

$$h_o(\mu_{x_i}) = \ln(\mu_{x_i} + r)$$
$$h_1(\mu_{x_i}) = r$$

Using equations (4.32) through (4.35) in equation (4.29) and substituting in equation (4.27) yields the results for $Z_l(E_1)$ which is needed to define the multigroup transfer matrices $\sigma_{l_{g\to j}}$ (equation (4.15)).

Finally, upon evaluating $\sigma_{l_{g\to j}}$, it is possible to calculate the number of particles released in group j as:

$$\Phi_{l_j} = \sum_{g=1}^{G} \sigma_{l_{g\to j}} \int_{E_{g-1}}^{E_g} \phi_l(E_1)\, dE_1 \quad (4.38)$$

4.3 Computer Implementation

A computer program PNNES was developed to evaluate the energy spectrum of neutrons produced from proton interactions with any structural material. The multigroup transfer matrices method described in the previous section was implemented in the program. Due to the lack of experimental data in the literature for the center of mass angular distribution $g[E_1, \eta_x(E_1, E_x)]$ for most nuclides, an isotropic center of mass angular distribution was considered. The isotropic center of mass angular distribution was obtained by using equation (4.18) with $a_i = 1/2$ and $b_i = 0$ [60]. Also, the calculations were only done for the $l = 0$ matrices.

The program is linked to a cross section data library. In the library, experimental cross section data for protons (with energy $\simeq$ 14.7 MeV) interacting with 65 naturally occurring isotopes of 36 target elements are found. Since all protons in this study are assumed to have an energy of 14.7 MeV (a conservative assumption), a cross section of 200 mb was assumed for any other nuclide for which no experimental cross section data was available. Every possible (p,n) reaction leading to the formation of either a ground or an isomeric state was considered. The reaction threshold energies for all target nuclides were taken from reference [48]. The program gives the energy spectrum of the produced neutrons in a 46 neutron energy group structure. The upper energy limit of the first group is 14.918 MeV, and the lower limit of the

last group is .022 eV. The energy limits of this group structure are given in Table (4.1). This neutron spectrum can be used to generate the neutron flux in the different reactor zones for activation calculations by using a neutron transport code.

Group	E (Top)	E (Low)	E (Midpoint)
1	1.4918E+07	1.3499E+07	1.4209E+07
2	1.3499E+07	1.2214E+07	1.2857E+07
3	1.2214E+07	1.1052E+07	1.1633E+07
4	1.1052E+07	1.0000E+07	1.0526E+07
5	1.0000E+07	9.0484E+06	9.5242E+06
6	9.0484E+06	8.1873E+06	8.6179E+06
7	8.1873E+06	7.4082E+06	7.7978E+06
8	7.4082E+06	6.7032E+06	7.0557E+06
9	6.7032E+06	6.0653E+06	6.3843E+06
10	6.0653E+06	5.4881E+06	5.7767E+06
11	5.4881E+06	4.9659E+06	5.2270E+06
12	4.9659E+06	4.4933E+06	4.7296E+06
13	4.4933E+06	4.0657E+06	4.2795E+06
14	4.0657E+06	3.6788E+06	3.8723E+06
15	3.6788E+06	3.3287E+06	3.5038E+06
16	3.3287E+06	3.0119E+06	3.1703E+06
17	3.0119E+06	2.7253E+06	2.8686E+06
18	2.7253E+06	2.4460E+06	2.5857E+06
19	2.4460E+06	1.8268E+06	2.1364E+06
20	1.8268E+06	1.3534E+06	1.5901E+06
21	1.3534E+06	1.0026E+06	1.1780E+06
22	1.0026E+06	7.4274E+05	8.7267E+05
23	7.4274E+05	5.5023E+05	6.4649E+05
24	5.5023E+05	4.0762E+05	4.7893E+05
25	4.0762E+05	3.0197E+05	3.5480E+05
26	3.0197E+05	2.2371E+05	2.6284E+05
27	2.2371E+05	1.6573E+05	1.9472E+05
28	1.6573E+05	1.2277E+05	1.4425E+05
29	1.2277E+05	6.7379E+04	9.5075E+04
30	6.7379E+04	3.1828E+04	4.9604E+04
31	3.1828E+04	1.5034E+04	2.3431E+04
32	1.5034E+04	7.1017E+03	1.1068E+04
33	7.1017E+03	3.3546E+03	5.2282E+03
34	3.3546E+03	1.5846E+03	2.4696E+03
35	1.5846E+03	7.4852E+02	1.1666E+03
36	7.4852E+02	3.5358E+02	5.5105E+02
37	3.5358E+02	1.6702E+02	2.6030E+02
38	1.6702E+02	7.8893E+01	1.2296E+02
39	7.8893E+01	3.7267E+01	5.8080E+01
40	3.7267E+01	1.7603E+01	2.7435E+01
41	1.7603E+01	8.3153E+00	1.2959E+01
42	8.3153E+00	3.9379E+00	6.1266E+00
43	3.9379E+00	1.8554E+00	2.8967E+00
44	1.8554E+00	8.7643E-01	1.3659E+00
45	8.7643E-01	4.1399E-01	6.4521E-01
46	4.1399E-01	2.2000E-02	2.1800E-01

Table 4.1: Energy Multigroup Structure in eV Group Limits.

Chapter 5

Activation and Safety Analysis for the D-^{3}He Fueled Tokamak Reactor Apollo-L2

5.1 Introduction

Apollo-L2 is a D-^{3}He fueled tokamak reactor design that utilizes direct conversion. The reactor has a major radius of 7.43 m and an aspect ratio of 4 [61]. The design considers operation for 30 full power years and would produce a net electric power of 1200 MW_e; the peak neutron wall loadings on the inboard and outboard sides of the midplane are 0.1 and 0.14 MW/m^2, respectively. Only 5 % of the 14.7 MeV protons produced in the plasma are assumed to strike the reactor first wall [62]. The inboard shield thickness is 56.5 cm and the outboard shield thickness is 76.5 cm. The shield is made of

steel and cooled with water.

Since the level of induced radioactivity in any fusion reactor depends on the type of alloy used as a structural material, three different steel alloys were chosen to study the impact of material selection on the level of induced radioactivity in Apollo-L2. The first steel alloy used is 316 SS which is the primary candidate structural material for the International Thermonuclear Experimental Reactor (ITER). The two other steel alloys considered in this study are PCA and the low activation austenitic steel Tenelon. Both are commonly used as structural materials in previous conceptual fusion reactor designs.

In this chapter a comparison of radioactivity and its related quantities, *i.e.*, the decay heat and the biological hazard potential (BHP), after shutdown for the three steel alloys in Apollo-L2 is presented. Results from the activation calculations were used to evaluate the waste disposal ratings (WDR) for the different structural materials considered. Calculations to determine the biological dose rate after shutdown at the back of the shield and at the back of the magnet were performed. In addition, the decay heat results were used to determine the thermal response of the shield following a loss of coolant accident (LOCA).

5.2 Calculational Procedure

Calculations for a one-dimensional toroidal cylindrical geometry model were conducted using the DKR-ICF computer code [40] with activation cross sections taken from the ACTL [36] library, and for 30 full power years (FPY) of reactor operation. The neutron transmutation data is given in 46 group structure format. The decay and gamma source data is taken from the table of isotopes with the gamma source data being in 21 group structure format. The (p,n) neutron energy spectrum was calculated by using the PNNES computer program. Both neutron fluxes (from fusion and (p,n) reaction) used for activation calculations were generated by the one-dimensional discrete ordinates neutron transport code ONEDANT [63] using the ENDF/B-V cross section data. The radial build used in both the neutronics and activation calculations is shown in Figure (5.1). Values from the proton-induced thick-target radionuclide activation yield library were used to calculate the proton-induced activity in the first wall (Tenelon) of the reactor. The PIAC computer program was used to perform the calculations. A flow chart of the computational procedure is shown in Figure (5.2).

The activation results were utilized in the radwaste classification performed using the WDR [64] computer code. The gamma decay source file generated by the DKR-ICF code was used to calculate the biological dose rate using the DOSE [40] code. In addition, the computer code ATHENA

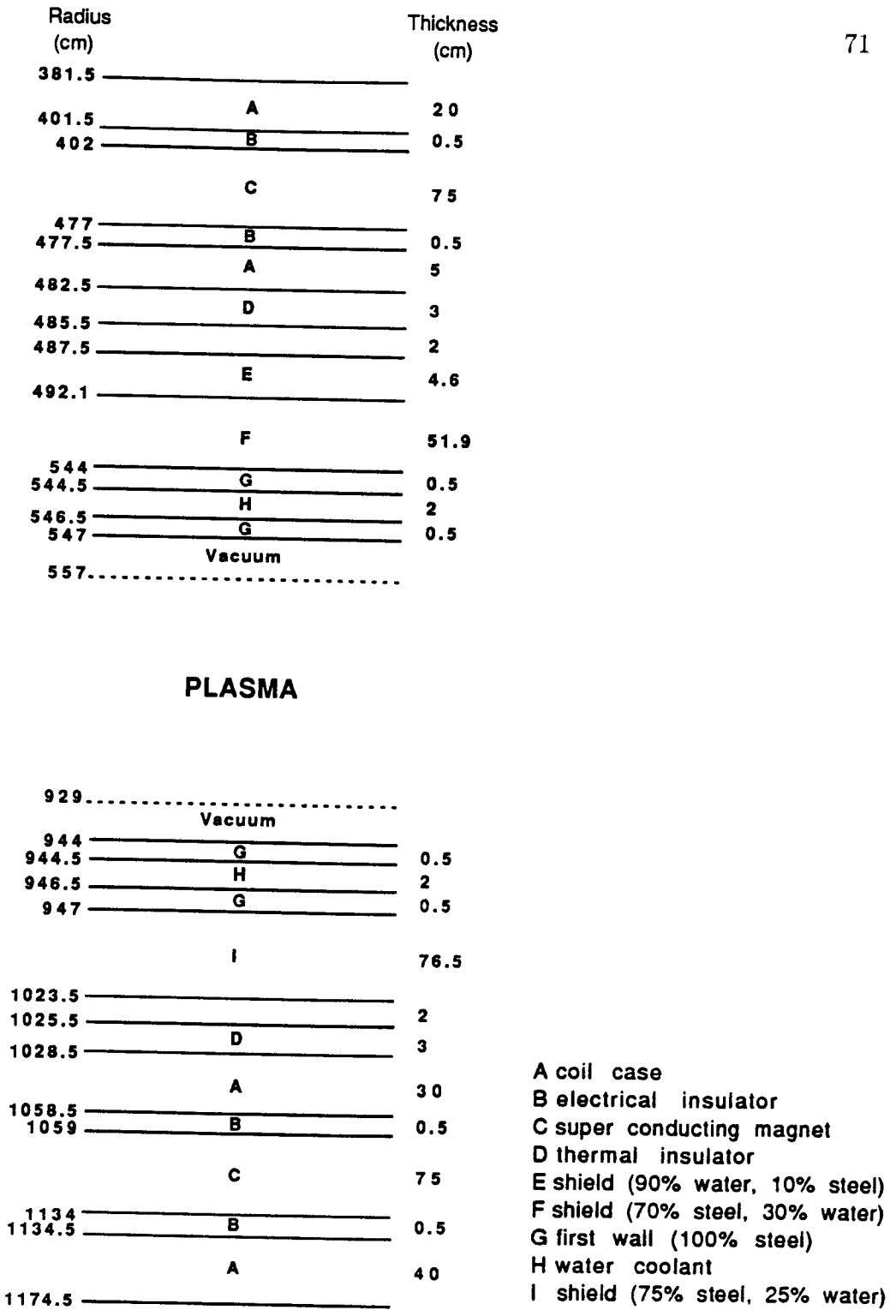

Figure 5.1: Radial build used in neutronics and activation calculations.

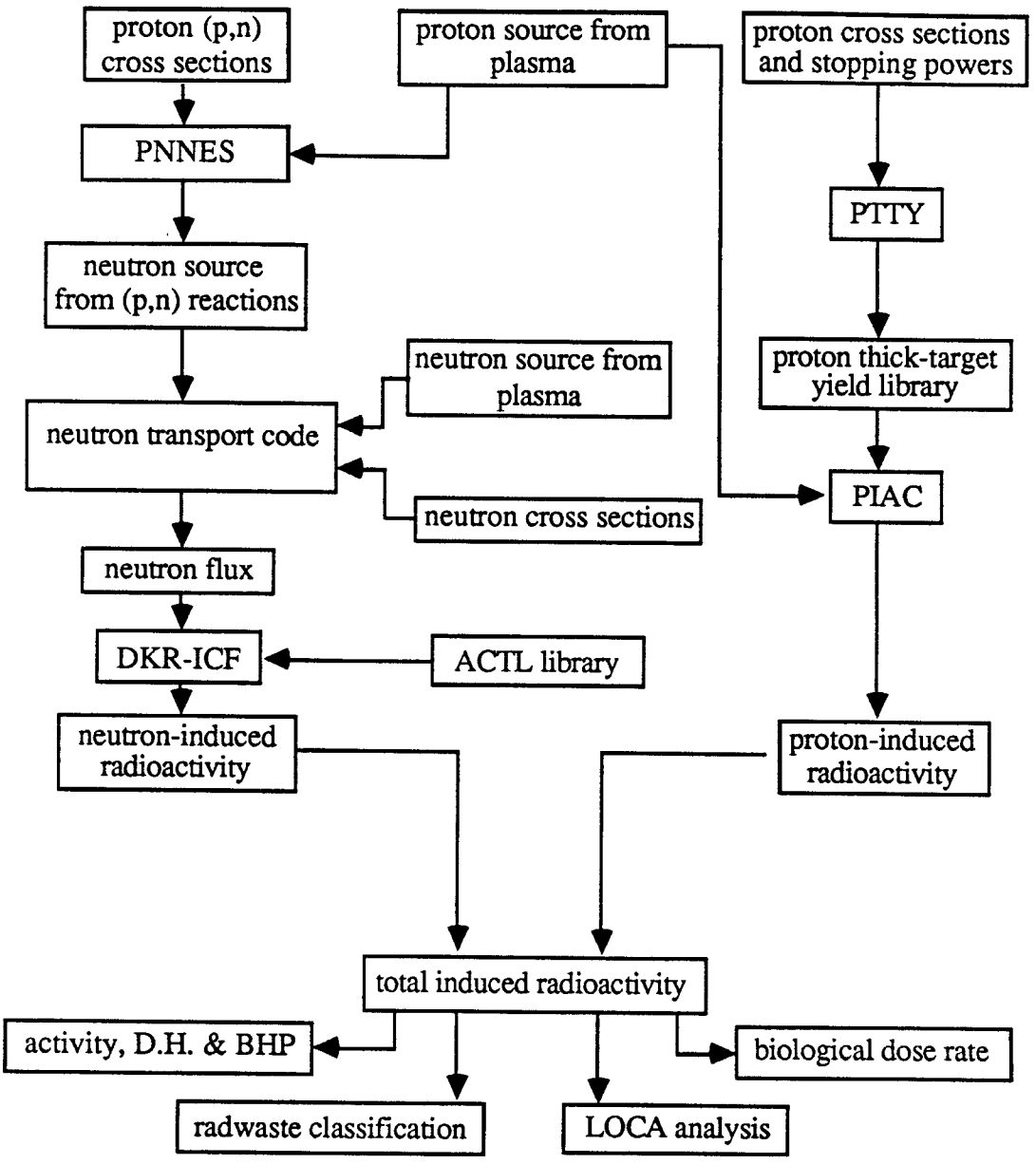

Figure 5.2: Flow Chart of the Computational Procedures.

[65] was used to determine the thermal response of the shield following a loss of coolant accident (LOCA) by utilizing the decay heat results. PCA, 316 SS and Tenelon were considered as structural materials. The composition of these materials is that presented in the Blanket Comparison and Selection Study (BCSS) report [66].

5.3 Comparison Between Proton and Neutron Induced Radioactivity

A comparison between the proton-induced and fusion neutron-induced radioactivity was conducted for a first wall made of the low activation austenitic steel Tenelon.

The calculations showed that while proton-induced activity (a result of proton direct interactions with the first wall) might add a very small contribution to the fusion neutron-induced activity for short-term (< 5 years) and mid-term (< 10 years) activities after shutdown, its contribution to long-term activity is negligible when compared to the activity induced by fusion neutrons in the reactor first wall. The short-term induced activity is dominated by ^{56}Mn($T_{1/2}$ = 2.6 hr), ^{54}Mn($T_{1/2}$ = 313 day), ^{55}Fe($T_{1/2}$ = 2.7 yr) and ^{51}Cr($T_{1/2}$ = 27.7 day) in case of fusion neutrons. In the case of proton-induced activity the major contributors are ^{56}Co($T_{1/2}$ = 78.5 day) pro-

duced from ^{56}Fe, ^{57}Co($T_{1/2}$ = 271 day) produced from ^{57}Fe and ^{60}Ni, ^{52}Mn($T_{1/2}$ = 5.63 day) and ^{52m}Mn($T_{1/2}$ = 21.4 min) produced from ^{52}Cr, ^{54}Mn produced from ^{54}Cr and ^{55}Fe produced from ^{55}Mn. While ^{57}Co is produced through (p,n) and (p,α) reactions, other contributors to the proton-induced activity are mainly produced through (p,n) reactions. In the period between 5 years and 10 years after shutdown, ^{55}Fe, ^{54}Mn, ^{63}Ni($T_{1/2}$ = 100 yr) and ^{60}Co($T_{1/2}$ = 5.7 yr) represent the major contributors to the fusion neutron-induced activity. For the same period of time, proton-induced activity is dominated by ^{55}Fe, ^{57}Co and ^{54}Mn. The long-term activity is only due to radionuclides produced from fusion neutron interactions with the reactor first wall such as ^{14}C($T_{1/2}$ = 5730 yr), ^{59}Ni($T_{1/2}$ = 80,000 yr) and ^{53}Mn($T_{1/2} = 3.8 \times 10^6$ yr). A Comparison between proton and fusion neutron induced specific activity as a function of time following shutdown is shown in Figure (5.3). Similar conclusions can be drawn out of a biological hazard potential (BHP) comparison as BHP is dominated by the same radionuclides which dominate the level of induced activity.

Proton-induced decay heat is mostly produced by ^{52}Mn and ^{52m}Mn. Figure (5.4) shows a comparison for the specific decay heat generated following shutdown. A high fusion neutron-induced decay heat is generated in the first wall within the first eight hours following shutdown due to the high content of manganese in Tenelon. In the meanwhile, one can notice that proton-induced decay heat generated following shutdown can be neglected if compared to the

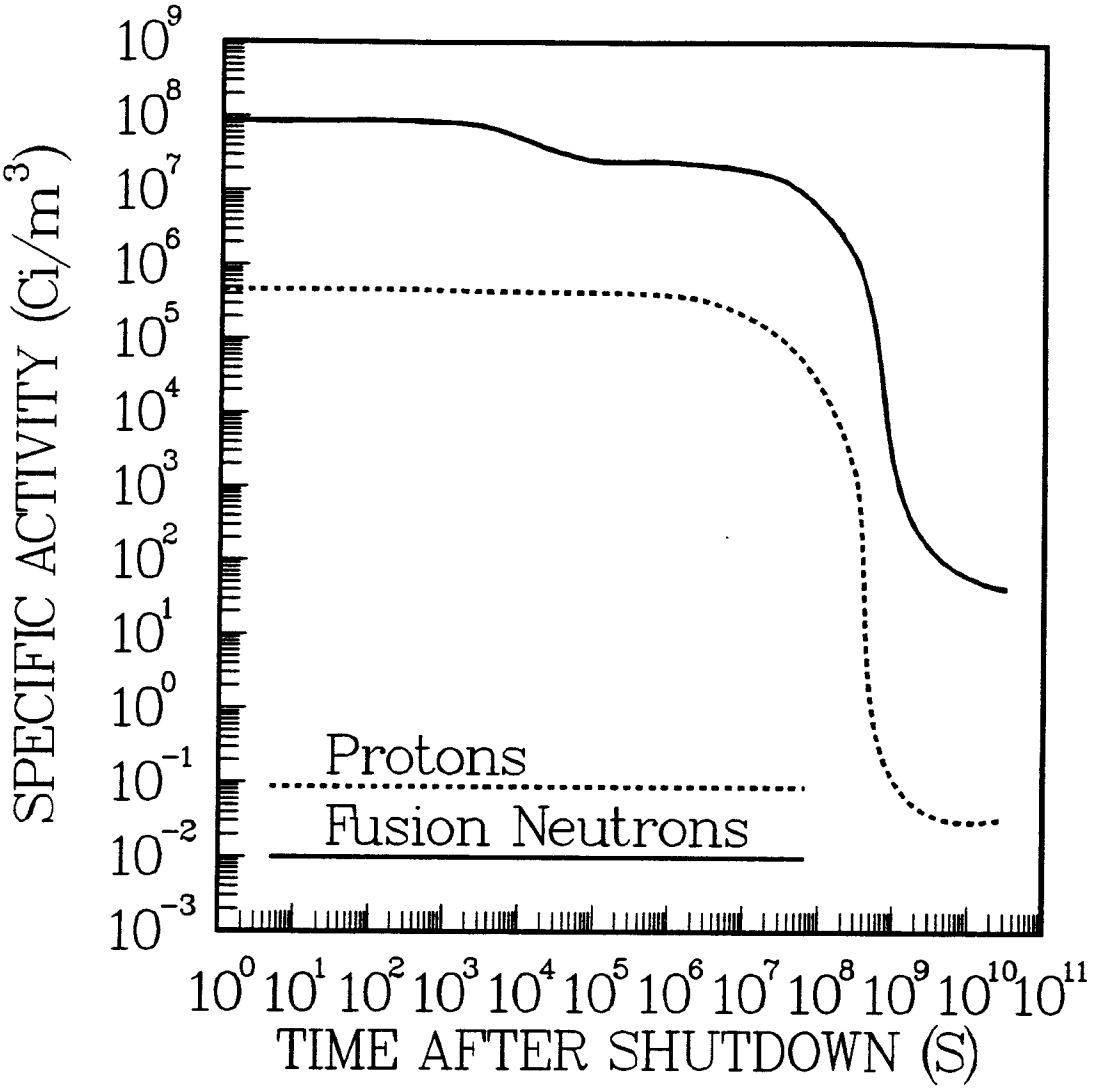

Figure 5.3: Comparison between proton and fusion neutron induced specific activity in the first wall of Apollo-L2.

fusion neutron-induced one.

Results obtained by the PNNES computer program showed that the (p,n) neutron flux is more than two orders of magnitude less than the fusion neutron flux. Figure (5.5) shows a comparison for the total activity induced in all zones of Apollo-L2 (with Tenelon structure) per cm height at the reactor's midplane. Similar to the differences in the two neutron fluxes, there is a two to three orders of magnitude difference in the level of induced-radioactivity.

The calculations also showed that even within the reactor first wall itself, the level of activity induced by the (p,n) neutrons is somewhat less than that induced by proton interactions with the wall structure at all times following shutdown. A comparison between the specific activity, decay heat and BHP generated in the first wall by fusion neutrons and protons & (p,n) neutrons are shown in Figures (5.6), (5.7) and (5.8), respectively. The fusion neutrons induce about two orders of magnitude more activity at shutdown than both protons and (p,n) neutrons produce combined together. One day after shutdown, the fusion neutron-induced activity is still slightly more than an order of magnitude higher. The decay heat figure shows a two to three orders of magnitude difference at any time following shutdown. The biological hazard potential differences varied from one order of magnitude at shutdown to more than two orders of magnitude 10 years after shutdown in favor of the fusion neutrons.

A one source of concern about the accuracy of the results obtained was due

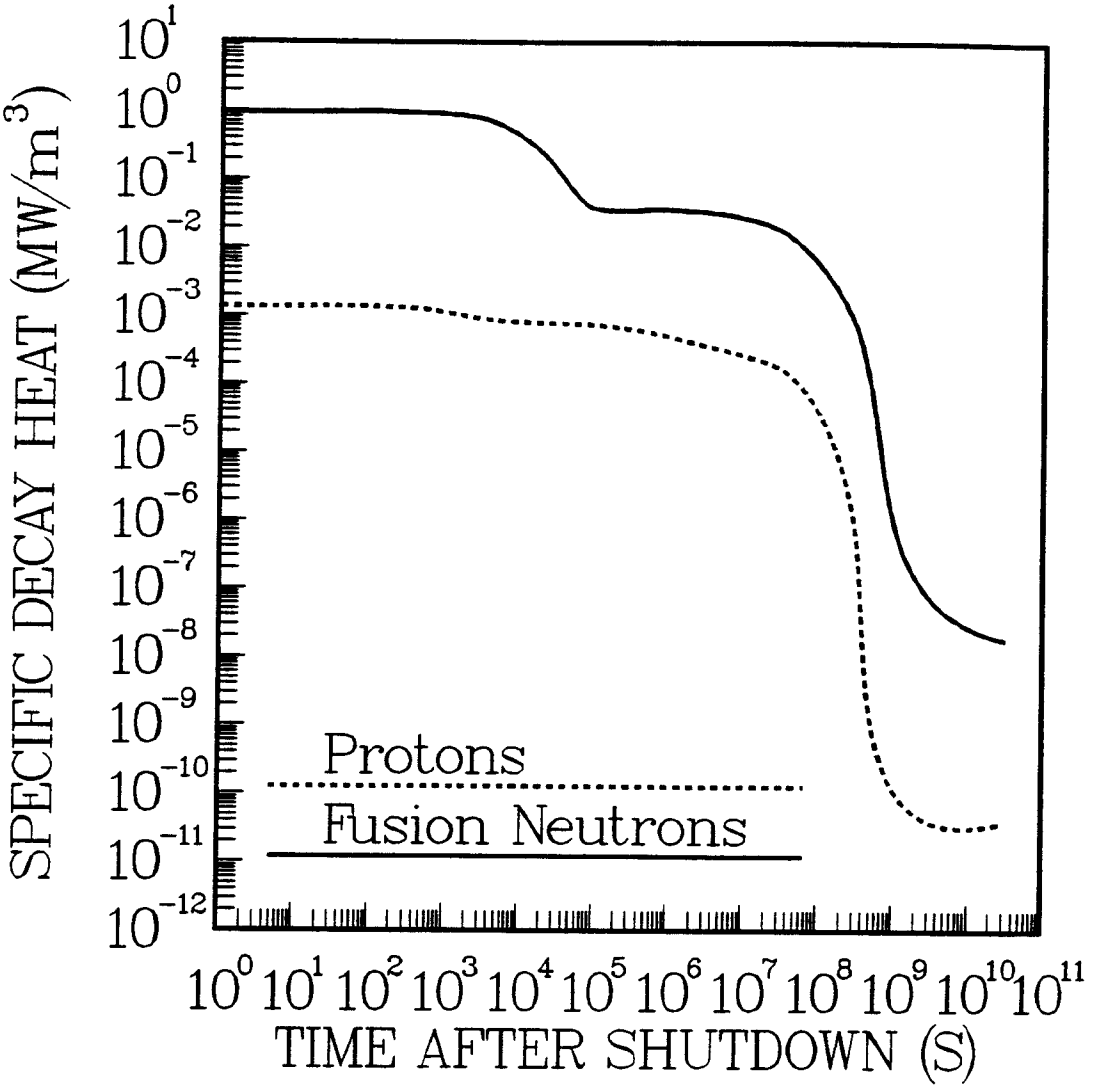

Figure 5.4: Comparison between the specific decay heat generated by protons and fusion neutrons in the first wall of Apollo-L2.

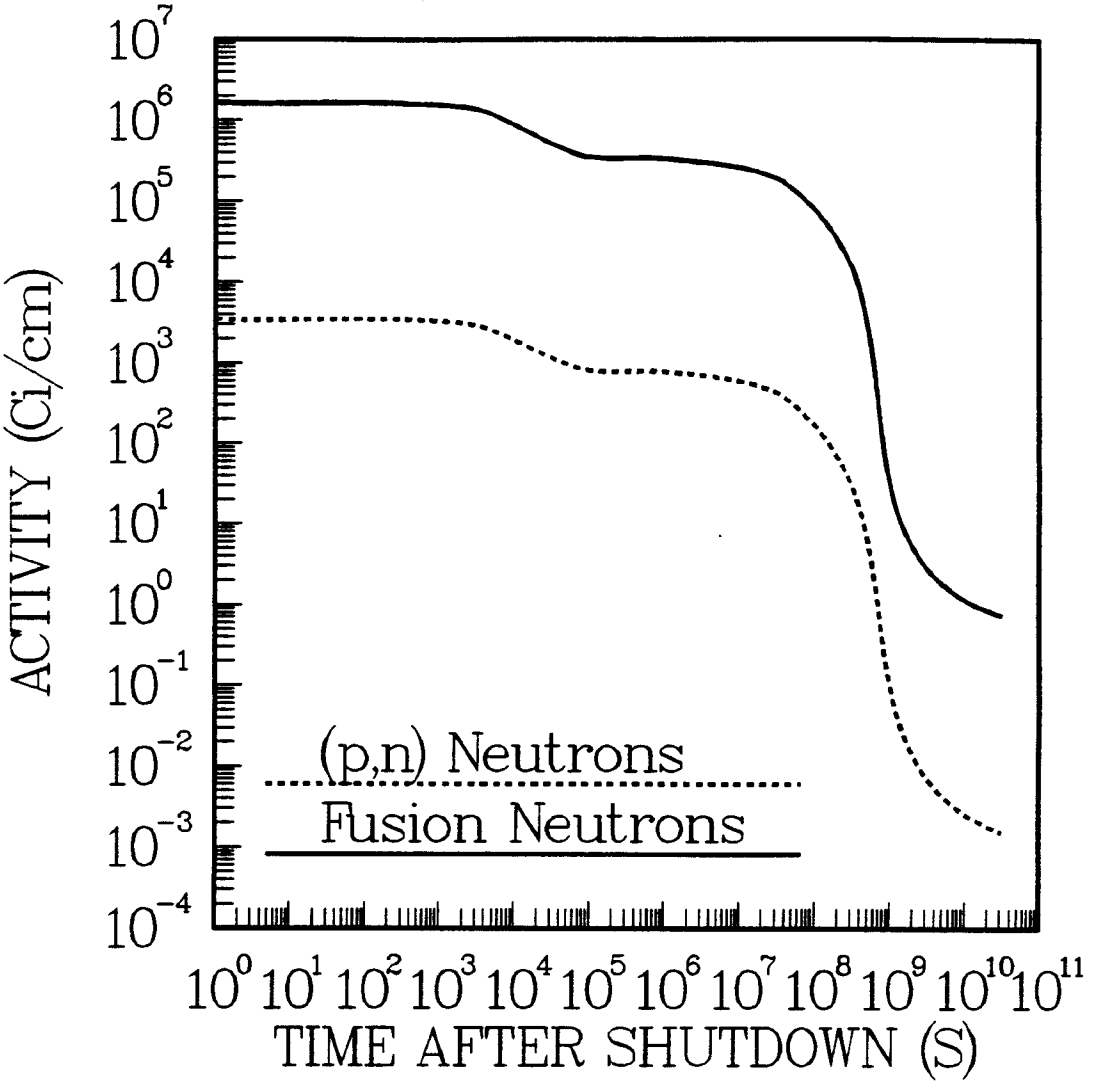

Figure 5.5: Comparison between the (p,n) and fusion neutron-induced activity in Apollo-L2.

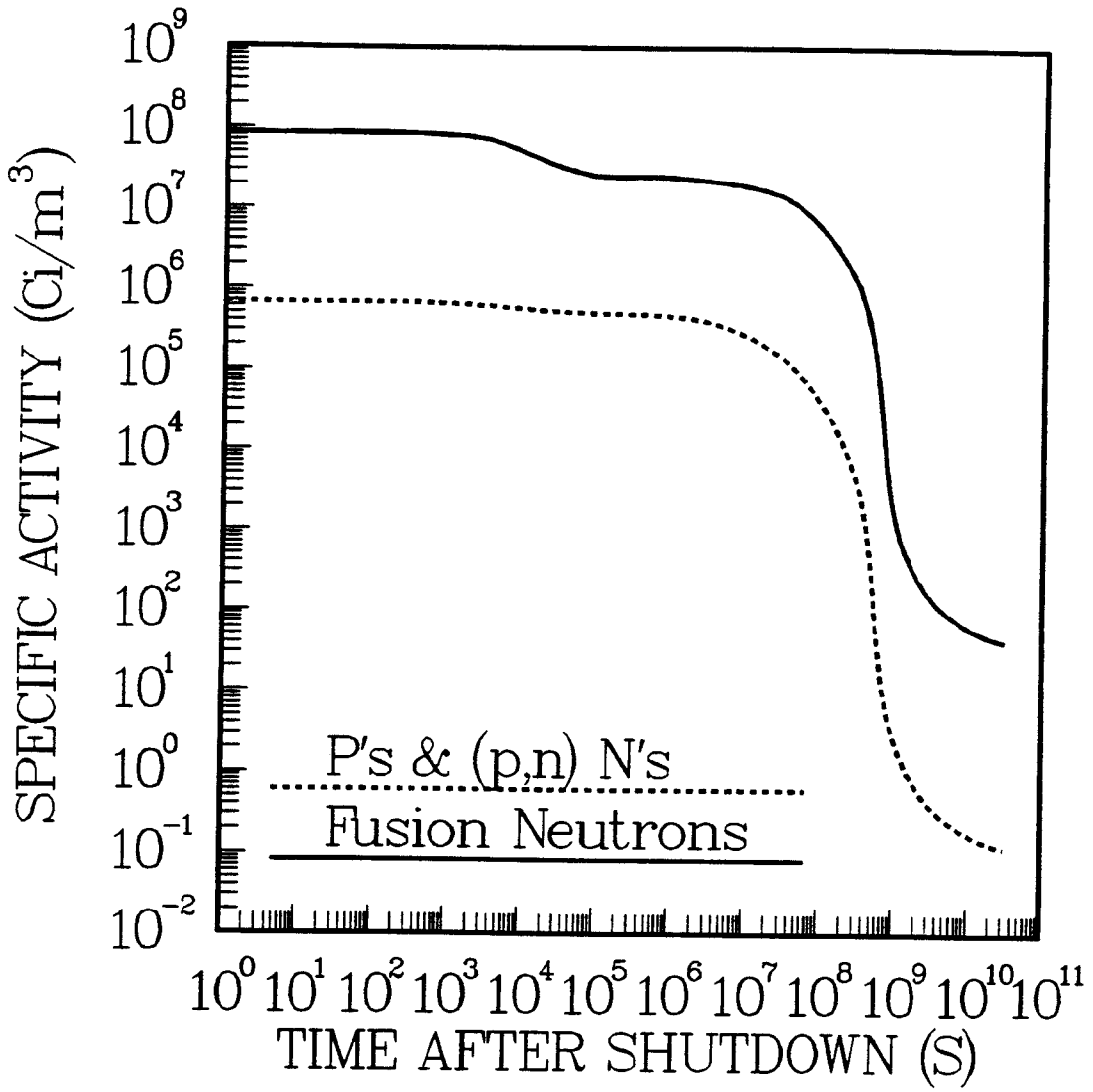

Figure 5.6: Protons & (p,n) neutrons vs. fusion neutrons induced specific activity in the first wall of Apollo-L2.

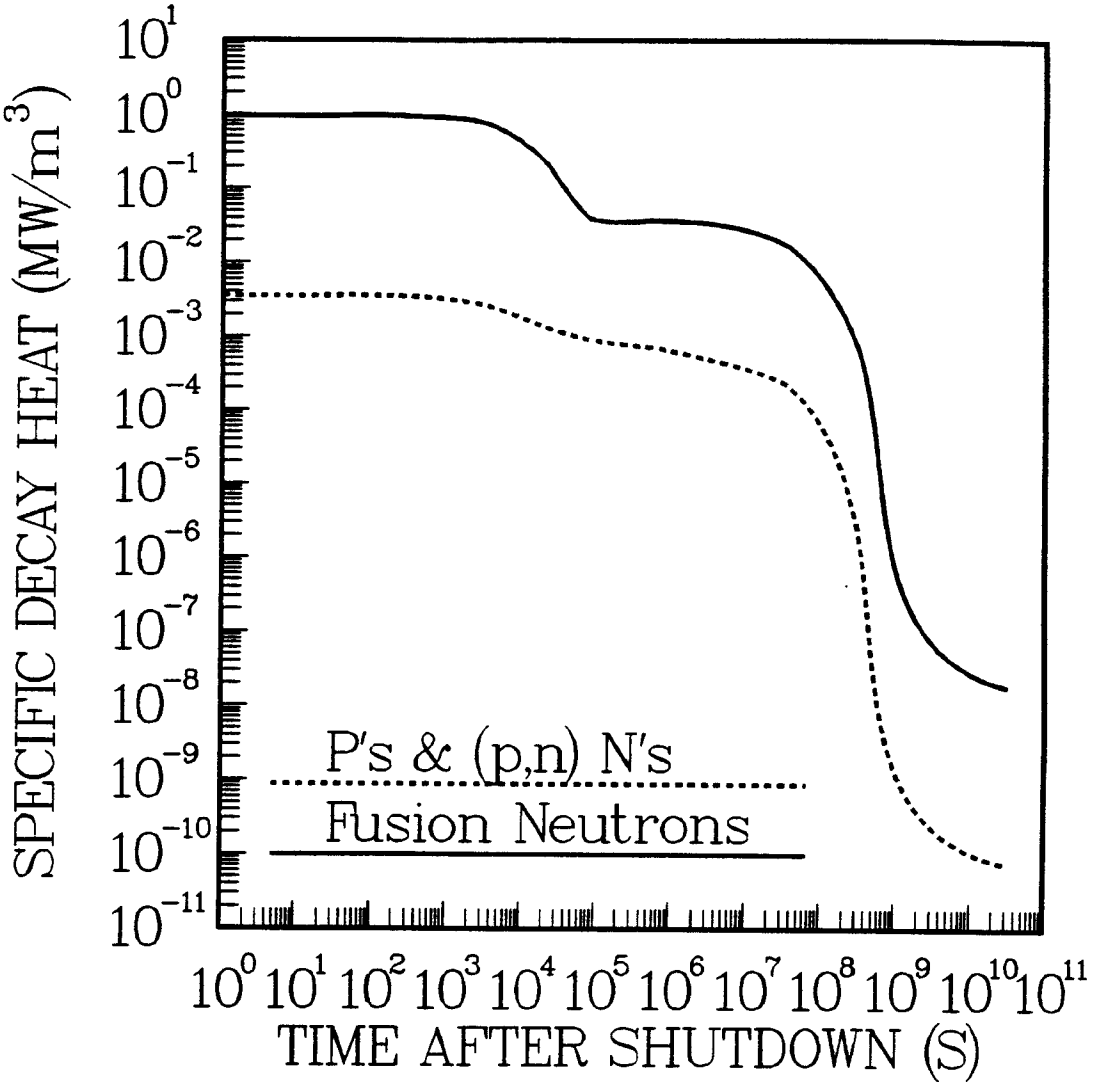

Figure 5.7: Specific decay heat generated by protons & (p,n) neutrons vs. fusion neutrons in the first wall of Apollo-L2.

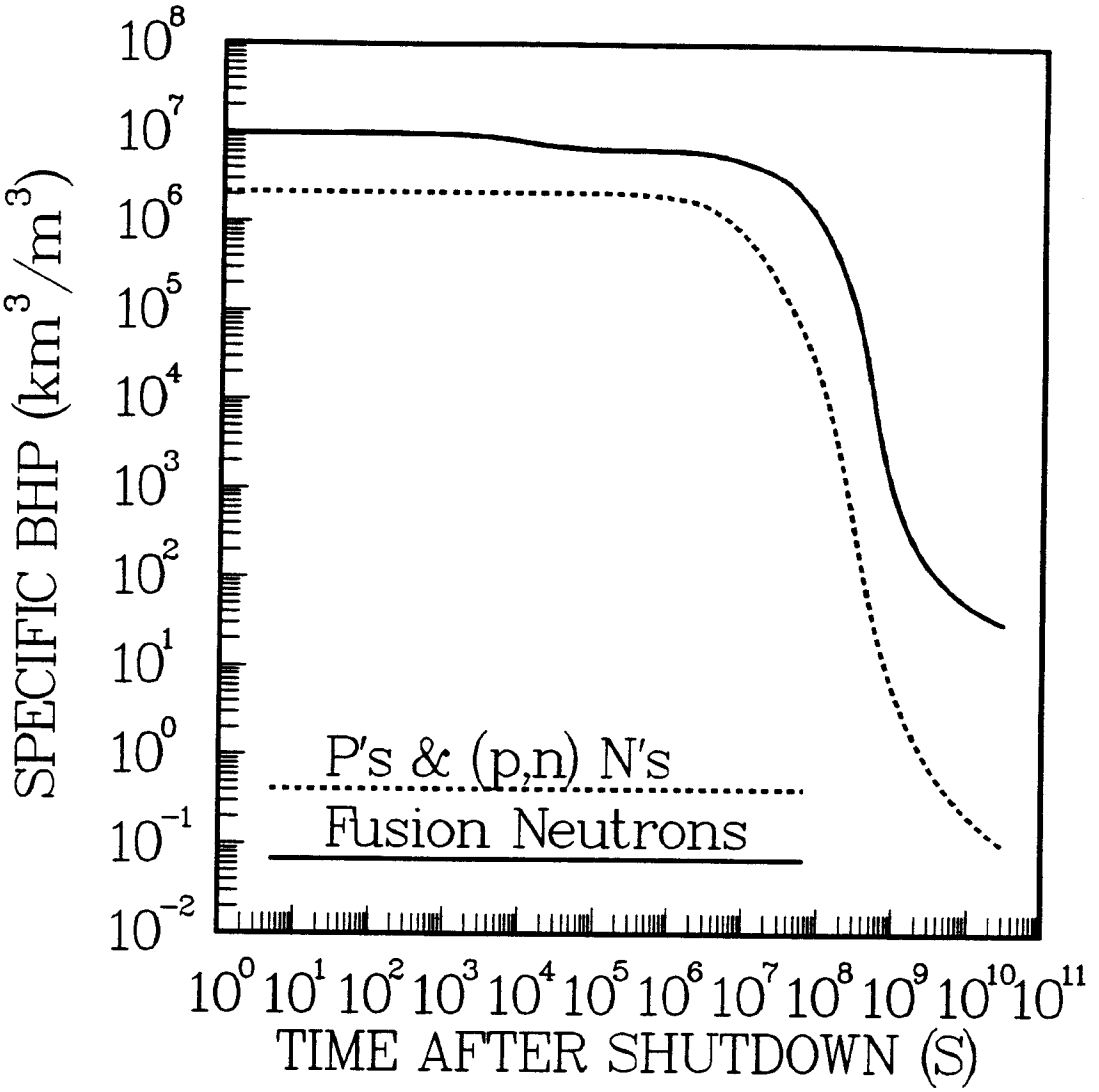

Figure 5.8: Protons & (p,n) neutrons vs. fusion neutrons induced specific biological hazard potential in the first wall of Apollo-L2.

to the fact that some of the experimental cross section data for the production of potential long-lived radioactive nuclides were not available. Another source of concern was that many of the available experimental cross section data were only for protons with energies that are several mega electron volts less than 14.7 MeV. To account for the effect of all radioactive nuclides, a conservative estimate of 200 mb (for 14.7 MeV protons undergoing (p,n) reactions) was assumed for each of the unavailable cross sections. New thick-target yield values were calculated by the PTTY computer program. The thick-target yield values were used by the PIAC computer program to calculate new estimated values for the activity, decay heat and BHP induced by protons in the reactor first wall. A comparison between the different results obtained by using experimental vs. experimental & estimated cross section data shows, (Figures (5.9), (5.10) and (5.11), respectively), a very mild increase in the estimated values over the values calculated by using the only available experimental cross section data. The estimated values were only less than a factor of two higher than the experimental ones within the first year following shutdown. At 10 years after shutdown, the estimated values were about three times higher than the experimental ones. ^{55}Fe produced from ^{55}Mn is the dominant radionuclide within this period of time. The reason for the increase is that the experimental cross section data for the ^{55}Mn (p,n) reaction were only available for proton energies less than 8.1 MeV. The estimated values are about an order of magnitude higher in the period $\geq$

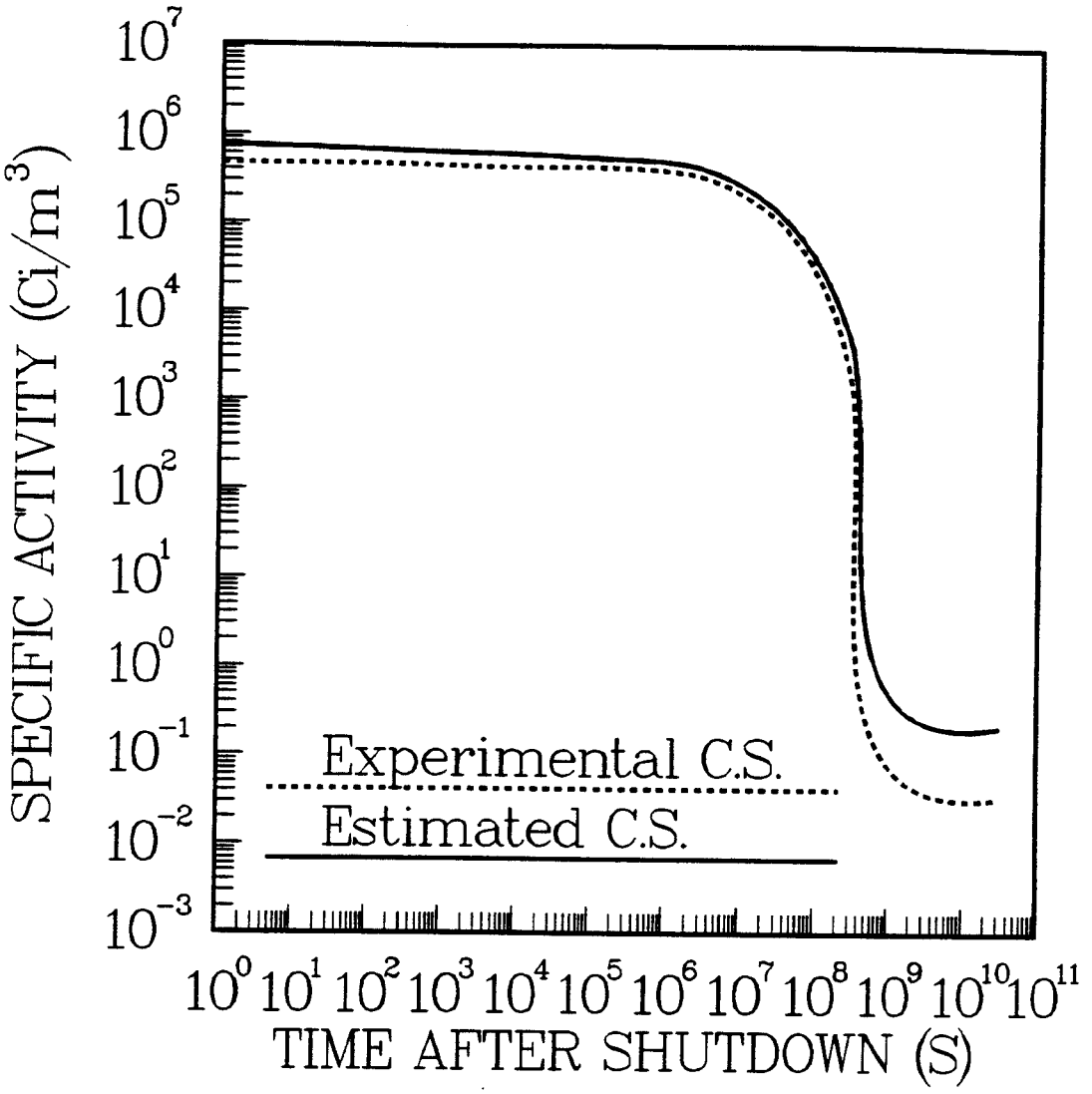

Figure 5.9: Comparison between proton-induced specific activity by using both experimental and estimated cross sections.

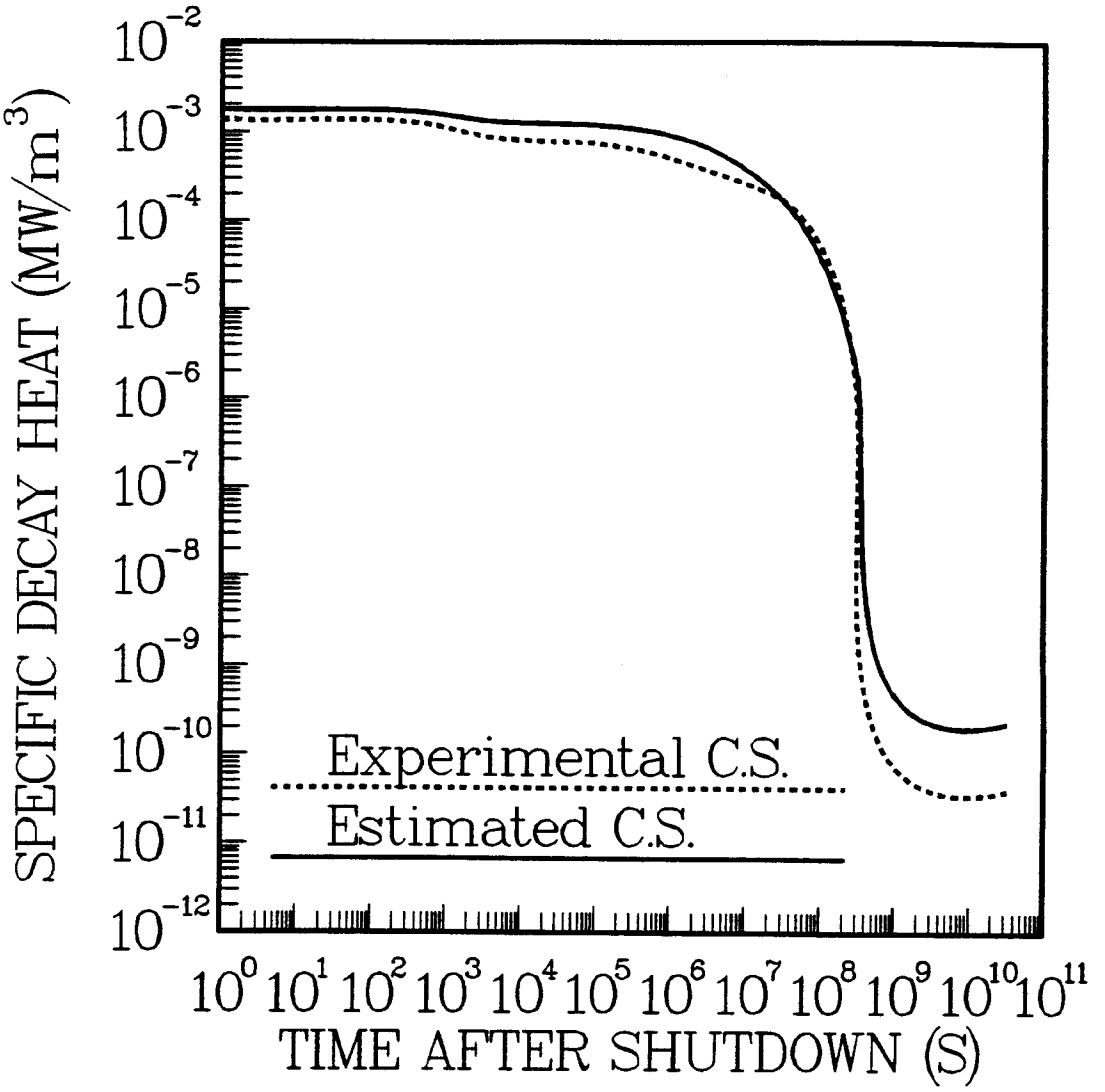

Figure 5.10: Comparison between the specific decay heat generated by protons by using both experimental and estimated cross sections.

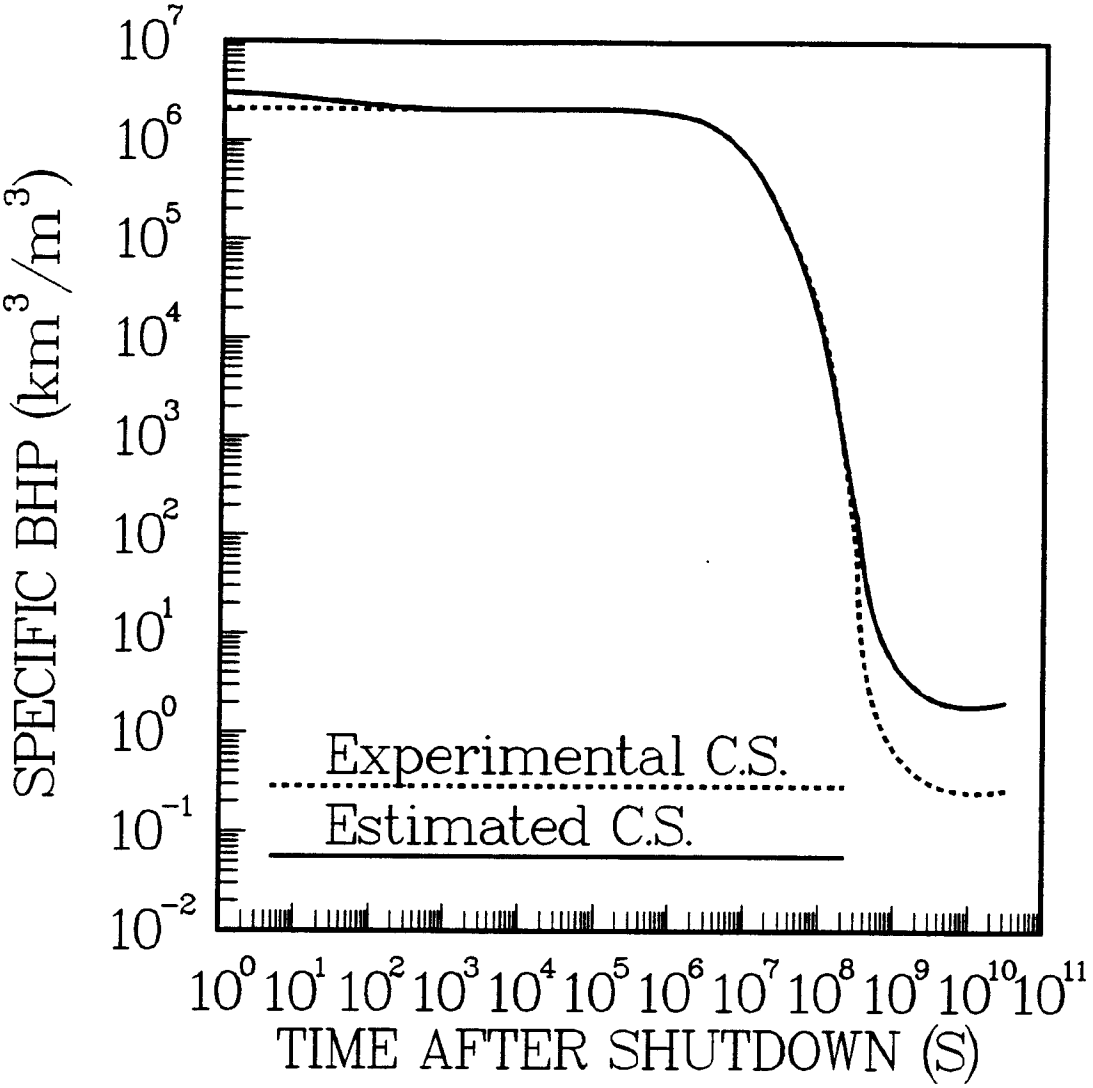

Figure 5.11: Comparison between proton-induced specific biological hazard potential by using both experimental and estimated cross sections.

100 years after shutdown. The major contributor is ^{53}Mn which is produced by the ^{53}Cr (p,n) reaction. The experimental cross section data for this reaction were only available for proton energies less than 5.88 MeV. However, the estimated value for the long-term activity is more than two orders of magnitude less than the fusion neutron-induced activity. More specifically, the ^{53}Mn contribution to the fusion neutron-induced activity is an order of magnitude higher than its contribution to the proton-induced one.

5.4 Results

5.4.1 Activity, Decay Heat and Biological Hazard Potential

The total activity in Apollo-L2 for the different steel alloys at shutdown is 438 MCi with PCA, 408 MCi with 316 SS and 939 MCi with Tenelon. In all three cases, the short-term activity after shutdown is dominated by ^{55}Fe, ^{56}Mn, ^{51}Cr and ^{54}Mn with ^{56}Mn and ^{54}Mn being the most dominant isotopes in the case of Tenelon. In the period between 1 year and 10 years after shutdown, ^{55}Fe and ^{54}Mn, in addition to ^{63}Ni and ^{60}Co, represent the major contributors in all cases. Finally, the long-term activity comes from ^{59}Ni, ^{93m}Nb($T_{1/2}$ = 13.6 yr), ^{93}Mo($T_{1/2}$ = 3500 yr), ^{14}C and ^{63}Ni, where ^{14}C is the major contributor by far if Tenelon is used as a structural material.

The total activity per cm height as a function of time following shutdown is shown in Figure (5.12) for the case of Tenelon. The results for the two other alloys show a similar trend. The outboard activity is higher than the inboard activity at all times following the reactor shutdown.

The decay heat generated in Apollo-L2 is almost dominated by the same isotopes that dominate the level of activity in the reactor after shutdown. If Tenelon is used as a structural material, as much as 96% of the afterheat generated at shutdown can be attributed to ^{56}Mn. A comparison between the total decay heat associated with different steel alloys is shown in Figure (5.13). While both PCA and 316 SS produce a comparable amount of decay heat, Tenelon results in a larger decay heat in the first 8 hours following shutdown due to its high manganese content. Decay heat generated in Tenelon starts to drop as ^{56}Mn starts to decay. Both PCA and 316 SS generate significantly larger amount of afterheat than Tenelon after about 3 years of reactor shutdown.

If Tenelon is used, the integrated decay heat generated during the first day after shutdown in Apollo-L2 is more than twice the level generated if PCA or 316 SS is used. Nevertheless, Tenelon generates a comparable amount of decay heat within a week. Figure (5.14) shows the effect of using the different steel alloys on the total integrated decay heat in Apollo-L2.

The biological hazard potential (BHP) associated with Tenelon structure is less than that with either PCA or 316 SS at all times following shutdown.

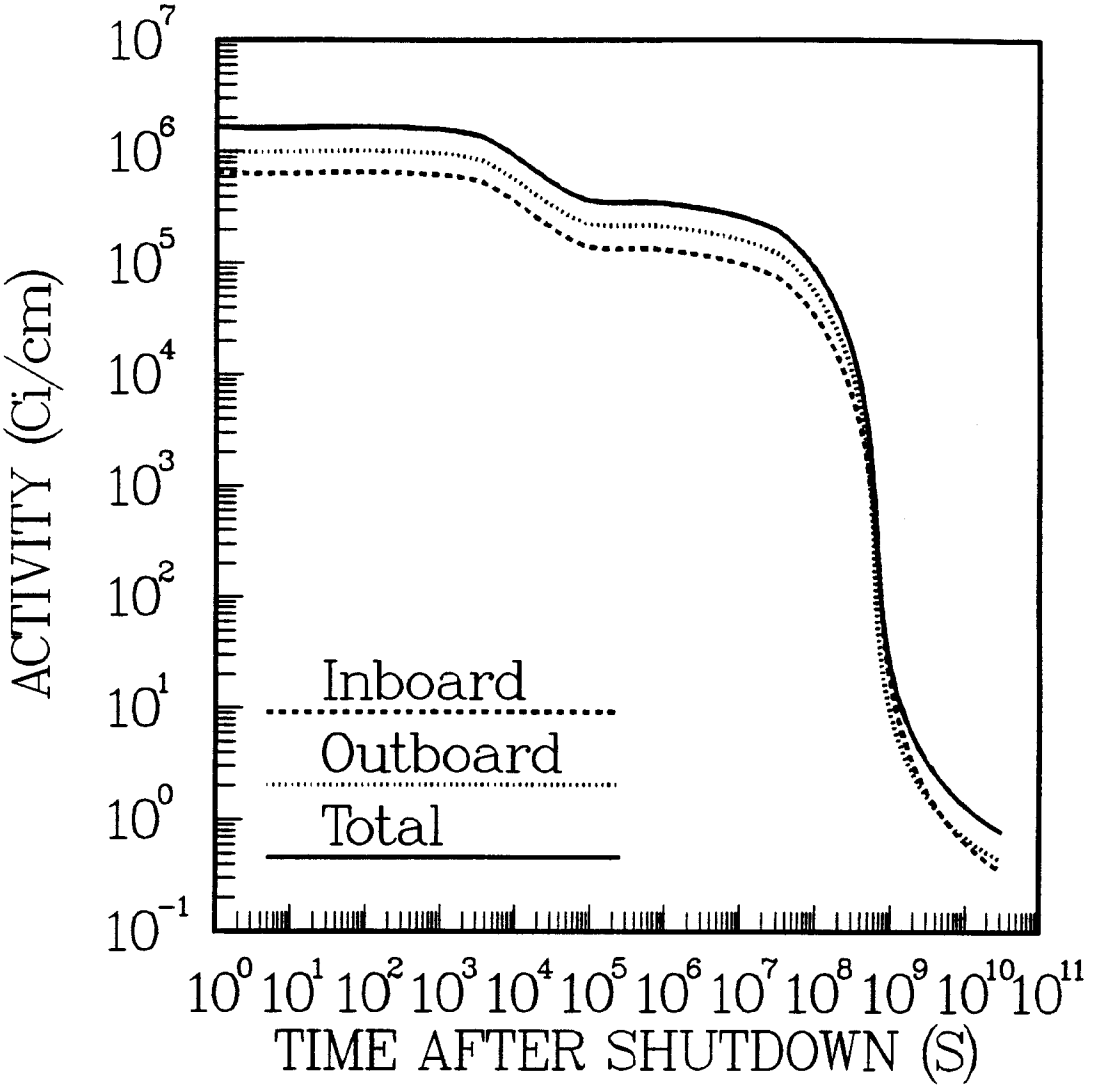

Figure 5.12: Activity per cm height at Apollo-L2's midplane using Tenelon.

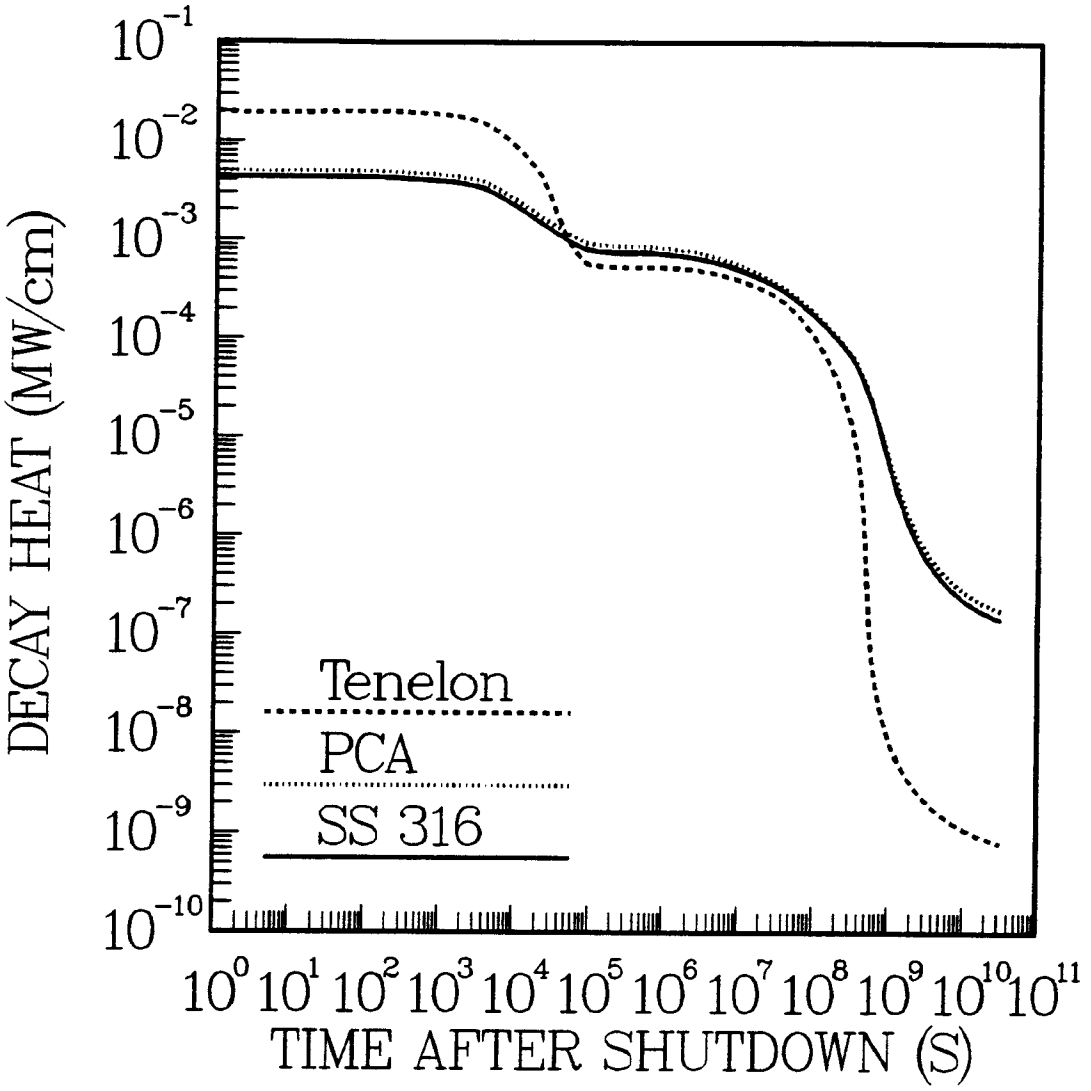

Figure 5.13: Comparison between decay heat generation for the different steel alloys used in Apollo-L2.

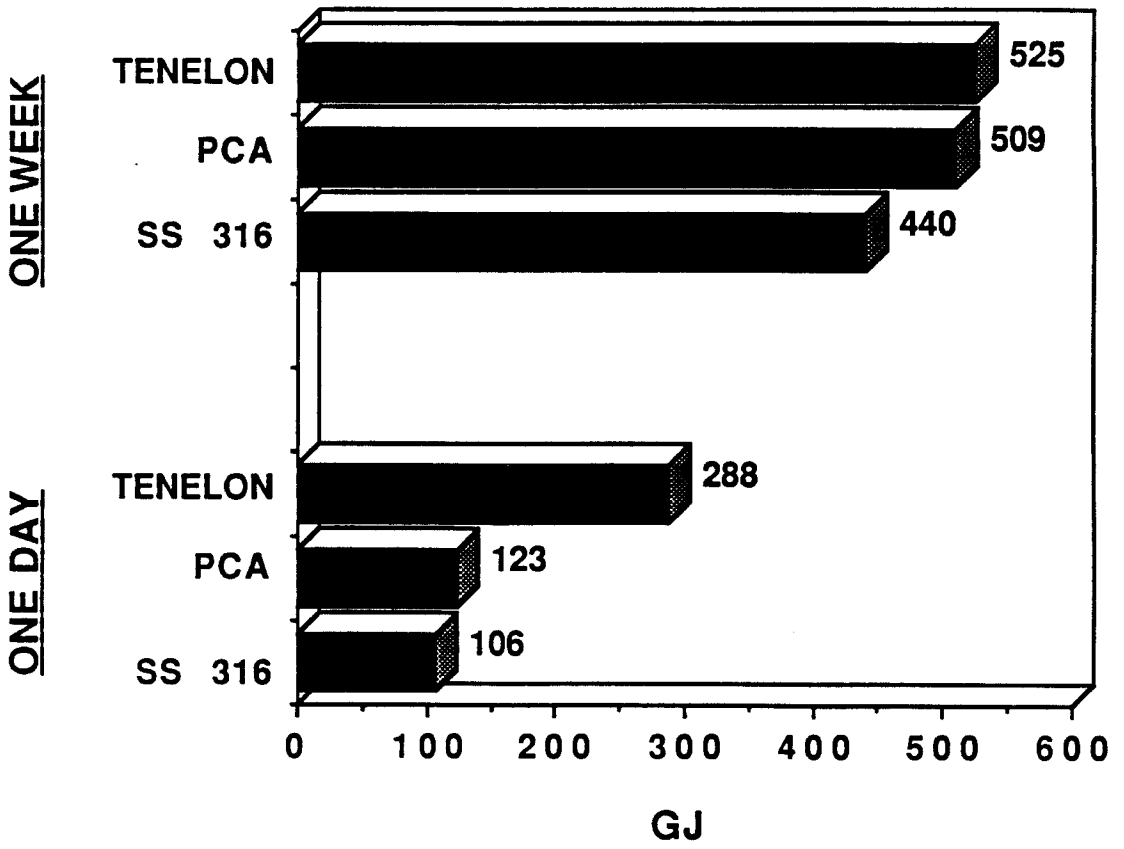

Figure 5.14: Integrated decay heat in Apollo-L2.

In general, the results obtained for the BHP show similar variation with time after shutdown as the activity and decay heat. The total BHP at shutdown is 9.24×10^7 km^3 air with PCA and 9.21×10^7 km^3 with Tenelon or type 316 SS.

5.4.2 Radwaste Classification

The radwaste of Apollo-L2's structure has been evaluated according to both 10CFR61 [67] and Fetter [68] waste disposal concentration limits (WDL). The different radionuclide specific activities calculated by the DKR-ICF code were used to calculate the waste disposal ratings after being normalized to the average inboard and outboard neutron wall loadings of 0.065 and 0.095 MW/m^2, respectively. The waste disposal ratings for class C low level waste (LLW) are given in Table (5.1) for the three different structural materials. The waste disposal rating (WDR) is defined [22] as the sum of the ratio of the concentration of a particular isotope to the maximum allowed concentration of that isotope taken all over isotopes. A WDR $\leq$ 1 implies that the radwaste qualifies for shallow land burial.

The results in the first three rows of the table are given separately for averaging the activities over the first wall and shield of the inboard, outboard and both inboard and outboard regions, respectively. In the last row, results are given for the waste disposal ratings for the case of disposing both the

WDR	Tenelon/H_2O Shield		PCA/H_2O Shield		316 SS/H_2O Shield	
	NRC	Fetter	NRC	Fetter	NRC	Fetter
IB FW and Shield (no magnet)	.034 (.021 ^{94}Nb, .0118 ^{14}C)	.0765–.0797 (.052 ^{108m}Ag, .021 ^{94}Nb)	9.577 (7.29 ^{94}Nb, 1.72 ^{63}Ni)	9.02–22.57 (7.29 ^{94}Nb, 1.5–15. ^{99}Tc)	3.231 (1.43 ^{63}Ni, 1.14 ^{94}Nb)	3.308–19.97 (1.14 ^{94}Nb, 1.8–18.5 ^{99}Tc)
OB FW and Shield (no magnet)	.023 (.015 ^{94}Nb, .0075 ^{14}C)	.052–.054 (.035 ^{108m}Ag, .015 ^{94}Nb)	6.46 (5.04 ^{94}Nb, 1.06 ^{63}Ni)	6.28–16.2 (5.04 ^{94}Nb, 1.1–10.9 ^{99}Tc)	2.1 (.887 ^{63}Ni, .79 ^{94}Nb)	2.35–14.54 (.79 ^{94}Nb, 1.4–13.6 ^{99}Tc)
IB and OB First Wall and Shield	.026 (.017 ^{94}Nb, .009 ^{14}C)	.059–.061 (.04 ^{108m}Ag, .017 ^{94}Nb)	7.346 (5.68 ^{94}Nb, 1.26 ^{63}Ni)	7.05–18 (5.68 ^{94}Nb, 1.2–12.2 ^{99}Tc)	2.42 (1.04 ^{63}Ni, .89 ^{94}Nb)	2.63–16.05 (.89 ^{94}Nb, 1.5–14.9 ^{99}Tc)
IB + OB (FW, shield and magnet)	.0815 (.078 ^{94}Nb, .003 ^{14}C)	.093–.094 (.078 ^{94}Nb, .014 ^{108m}Ag)	2.57 (2.01 ^{94}Nb, .42 ^{63}Ni)	2.47–6.18 (2.01 ^{94}Nb, .4–4.11 ^{99}Tc)	.9 .384 ^{94}Nb, .35 ^{63}Ni)	.97–5.54 (.38 ^{94}Nb, .5–5.1 ^{99}Tc)

Table 5.1: Class C Waste Disposal Rating for Apollo-L2 (No Compactness)

1 Year After Shutdown.

inboard and outboard regions together. The WDR range given corresponds to that provided by Fetter for the WDL of some of the radionuclides. Only Tenelon easily meets class C limits. With the exception of disposing the outboard region or the inboard and outboard regions of type 316 SS structure together, neither PCA nor 316 SS would qualify as class C waste.

Contribution from long lived radioactive nuclides produced by proton interactions with the reactor structure will have no effect on the waste classification. Long-lived radionuclides produced by neutron interactions with the structural materials are the only contributors. The major contributors to the proton-induced activity in Apollo-L2 are those with half-lives less than 5 years. Hence, their contribution to the waste disposal rating (WDR) is negligible as the 10CFR61 limits are only given for radionuclides with half-lives greater than 5 years. The major contributing radionuclides and their contributions are given in parenthesis for each case. In almost all cases, ^{94}Nb($T_{1/2} = 20,000$ yr), which is produced from ^{93}Nb or ^{94}Mo, is the major contributor regardless of which WDL are used. In the case of PCA and 316 SS the other major contributor is ^{63}Ni produced from ^{63}Cu if 10CFR61 limits are used, and ^{108m}Ag($T_{1/2} = 130$ yr) produced from ^{107}Ag if Fetter limits are used. The secondary major contributors in the case of Tenelon are ^{14}C produced from ^{13}C and ^{14}N, and ^{99}Tc($T_{1/2} = 2.1 \times 10^5$ yr) produced from ^{98}Mo if the 10CFR61 and Fetter limits are used, respectively.

5.4.3 Biological Dose Rate

The biological dose rate has been calculated as a function of time following shutdown at the back of both the outboard shield and magnet for the three steel alloys. The results showed that the dose rate at the back of the shield is too high to allow hands-on maintenance. In all cases, the dose is dominated by ^{56}Mn and ^{58}Co($T_{1/2}$ = 70.8 day) in the first few days. ^{54}Mn and ^{60}Co dominate the biological dose in the first few years following shutdown. Figure (5.15) shows a comparison between the different dose rates at the back of the outboard shield. Just as in the case of the decay heat (Fig. (5.13)), the initial shape of the curve exhibits the same behavior. The dose rate at shutdown associated with the Tenelon structure is 3 times higher than that associated with either the PCA or 316 SS structures. The crossover point occurs after about 8 hours following shutdown, with both the PCA and 316 SS dose exceeding the Tenelon dose level thereafter. The large drop in the Tenelon dose rate at about 8 hours following shutdown is the result of the decay of ^{56}Mn. The calculated dose rates at the back of the magnet at shutdown are 6.51, 6.77 and 5.35 μrem/hr for PCA, 316 SS and Tenelon structures, respectively.

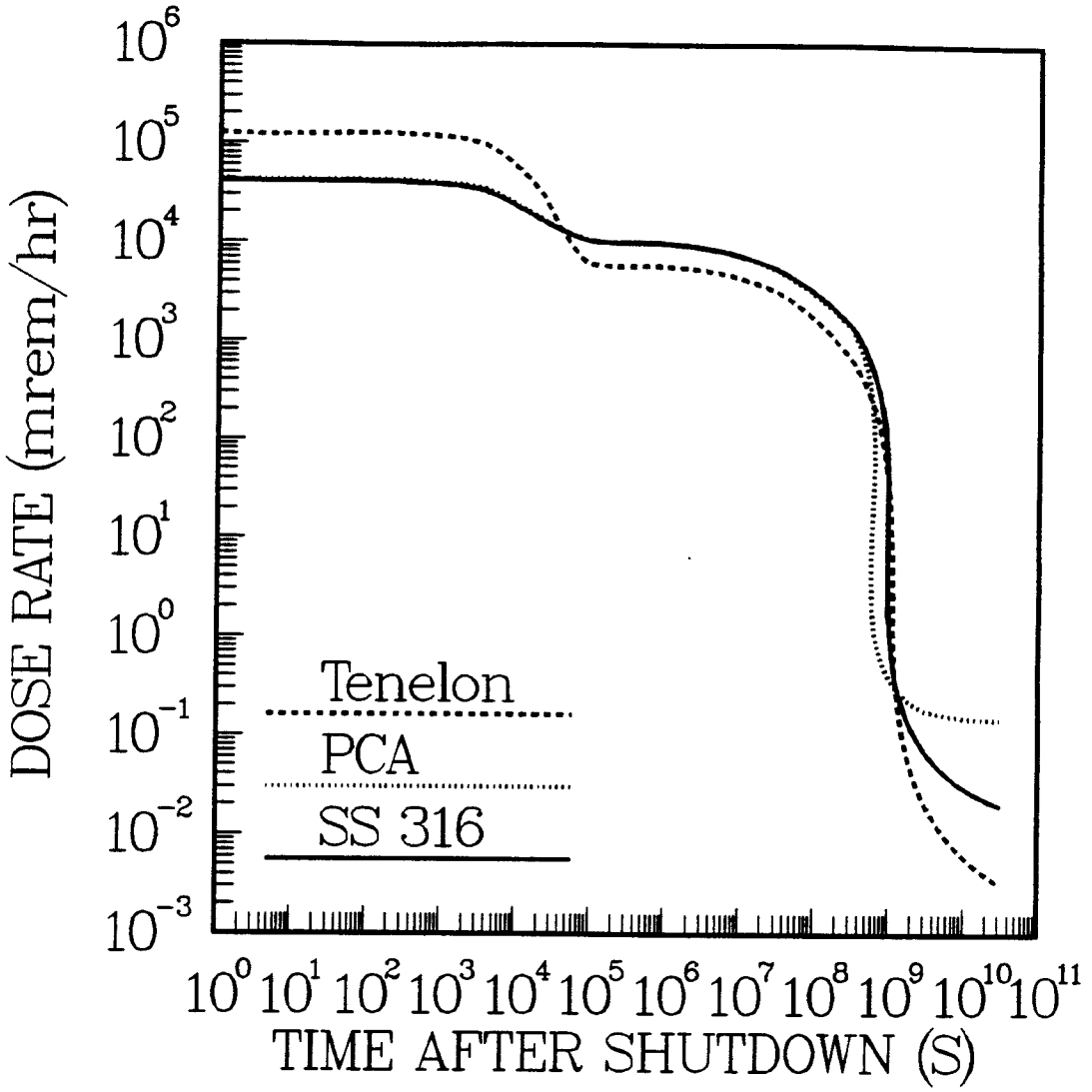

Figure 5.15: Comparison between dose rates at the back of the outboard shield.

5.4.4 LOCA Analysis

The temperature history during a loss of coolant accident (LOCA) in Apollo-L2 was analyzed using a one-dimensional thermal hydraulics computer code ATHENA [65]. In the analysis [69], the reactor was modeled as six heat conducting slabs (first wall, shield and magnet in each region) separated by five cooling ducts. The inboard and outboard regions are solved interactively assuming that all of the coolant channels and plasma volume are filled with air at atmospheric pressure. During the LOCA analysis, the coolant is assumed to be lost instantly and the plasma is assumed to stay on for 10 seconds. The initial operating temperature ranges from a high of 500°C at the first wall to about 400°C at the back of the shield. The inner legs of the superconducting TF coils are assumed to have an initial temperature of 4.2 K allowing the coils to act as a heat sink.

Figure (5.16) shows the temperature histories for the first wall and shield in both the inboard and outboard sides of the reactor for the case of Tenelon. In the first few hours following LOCA, one can notice that even though no sizable increase in the first wall temperature in both the inboard and outboard regions of Apollo-L2 have taken place, both the inboard and outboard shield temperatures start to rise slowly and the inboard shield temperature reaches a maximum increase of about 80°C within the first 8 hours following LOCA. This short-term increase in the shield temperature is due to the large

amount of decay heat generated by ^{56}Mn which has a half life of 2.6 hours. After one week, the average temperature ranges from a high of 200°C at the first wall of the inboard region to 150°C at the outboard shield.

A comparison between the first wall temperature as a function of time for the cases of PCA and Tenelon is shown in Figure (5.17). In the case of Tenelon, the first wall will exhibit a higher temperature than the PCA first wall up to five days after the plasma is turned off. The results show that two weeks after LOCA, the maximum inboard first wall temperatures are 468, 445 and 423 K for PCA, 316 SS and Tenelon structures, respectively.

5.4.5 Summary

The short-term levels of radioactivity, decay heat and biological hazard potential (BHP) associated with the use of Tenelon as a structural material in Apollo-L2 are comparatively higher than those found if PCA or type 316 SS is used instead. However, an Apollo-L2 structure made of Tenelon would easily qualify as class C low level waste (LLW) and hence would meet the U.S. requirements for shallow land burial. The high level of the biological dose rate following shutdown at the back of the outboard shield will only allow for remote maintenance. Assuming heat dissipation to the TF magnets only, all of the three steel alloys considered can withstand a loss of coolant accident (LOCA), with the maximum first wall temperature leveling off at

about 200°C in the two weeks following LOCA.

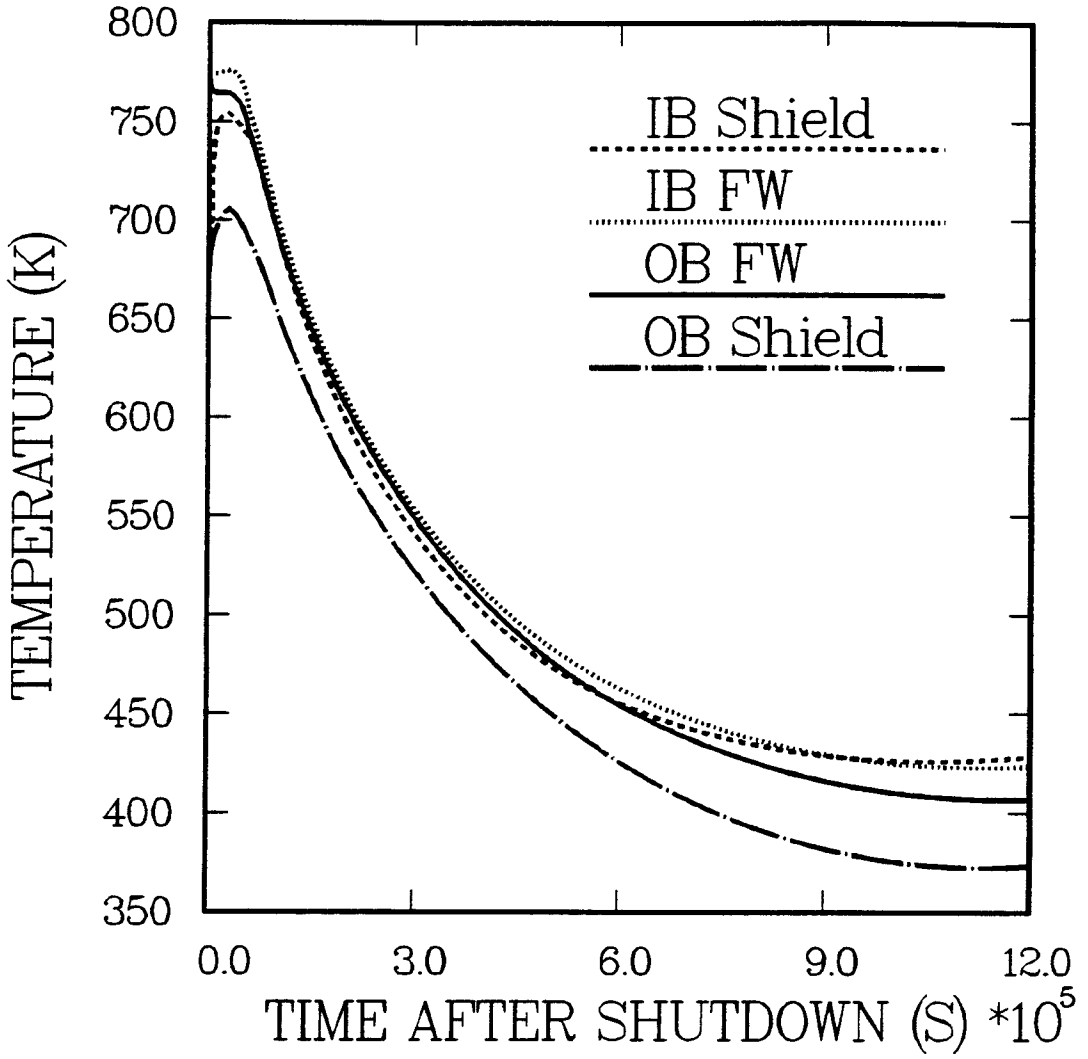

Figure 5.16: Temperature histories for the case of Tenelon.

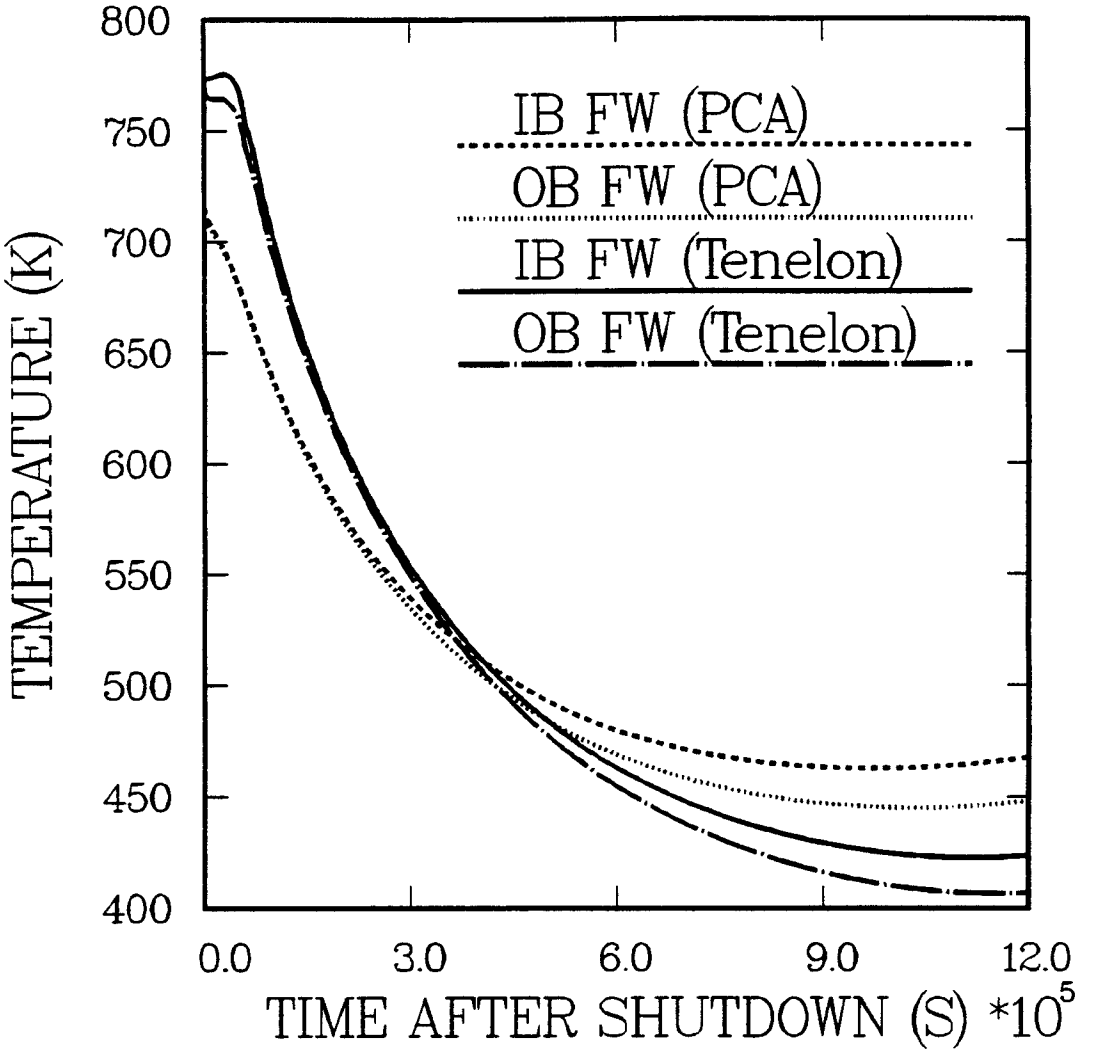

Figure 5.17: Comparison between the first wall temperature histories for the cases of PCA and Tenelon.

Chapter 6

Conclusions and Recommendations

This study aimed at investigating the effect of proton activation on the total level of activity induced in D-^{3}He fusion reactors. To reach this objective the following steps have been taken:

1. A computer program PTTY has been developed to produce a library that contains thick-target activation yields for radionuclides produced by proton interactions with several stable target elements. Proton energy-dependent cross sections were used along with proton stopping data to produce the library. Only experimental radionuclide production cross sections for (p,n), (p,γ), (p,2n), (p,α) and (p,pn) were used in the calculations. Data for protons ($E_p \leq 14.7$ MeV) interacting with 109 naturally occurring isotopes of 58 target elements were compiled. In its present form, the library contains thick-target yield data for 164

radioactive isotopes.

2. The thick-target yield library is linked to a second computer program PIAC that calculates proton-induced activity. The program calculates the activity, decay heat and biological hazard potential (BHP) induced in any given reactor structural material as a function of time after shutdown.

3. A third computer program PNNES that uses the available (p,n) experimental cross section data for 14.7 MeV protons to evaluate the potential neutron flux produced as a result of proton interactions with any structural material has been developed. Since such experimental cross section data are only available for 65 naturally occurring isotopes of 36 target elements, a cross section of 200 mb was used as a conservative assumption for all other nuclides. The program produces a neutron flux in a 46 neutron energy group structure that can be used with most of the available neutron transport codes.

4. A comprehensive activation and safety analysis study for a D-^{3}He tokamak fusion power reactor design (Apollo-L2) has been carried out. Three different steel alloys (PCA, 316 SS and Tenelon) were considered for use as structural materials. Thick-target yield values from the library were used to calculate the proton-induced activity in the first wall (Tenelon) of the reactor. In the meanwhile, 2.45 and 14.1 MeV

neutrons produced from the D-D and D-T secondary reactions as well as neutrons produced as a result of proton interactions with the reactor first wall (in 46 energy group structure) through (p,n) reactions were used in the neutron transport calculations to generate the neutron flux in the different reactor zones for the activation calculations.

The results showed that proton-induced activity represents a small fraction of the total radioactivity generated in the Tenelon structure. The proton-induced activity was more than two orders of magnitude less than the activity induced by the fusion neutrons at shutdown, and more than one order of magnitude less at about a day following shutdown. A decay heat comparison showed that there is two to three orders of magnitude difference in the level of decay heat generated by neutrons and protons at any time after shutdown. Fusion neutrons remain the main concern in any safety analysis in case of loss of coolant accident (LOCA).

A similar analysis for the effect of the activity induced by neutrons produced through the different (p,n) reactions in the Tenelon first wall showed that even though this new neutron source is generated within the reactor first wall itself, it still only results in a level of activity, decay heat and biological hazard potential which is slightly less than those induced by protons within the reactor first wall. The level of radioactivity induced by these (p,n) neutrons is two to three orders of magnitude less than fusion neutron-induced radioactivity at any time following shutdown.

The radwaste classification analysis indicated that the major contributors to the proton-induced activity in Apollo-L2 will have no noticeable effect on the level of waste classification. The reason is that proton-induced activity is mainly dominated by radioactive nuclides with half-lives less than five years. The Nuclear Regulatory Commission document 10CFR61 only gives waste disposal limits (WDL) to radioactive nuclides with half-lives more than five years. Added contribution from long-lived radioactive nuclides produced by proton interactions with the reactor structure is negligible if compared to the contribution given by the radionuclides produced as a result of neutron interactions. A similar conclusion is reached when it comes to estimating the effect protons will have on the biological dose rate outside the reactor as well as the thermal response of the reactor shield following a loss of coolant accident.

As one final step in the analysis, a cross section of 200 mb (a conservative assumption) was assumed for any nuclide with no available experimental cross section data for 14.7 MeV protons. New thick-target yield values were calculated and used in estimating a new level of proton-induced activity. Results of the analysis showed a very mild increase in the level of activity, decay heat or biological hazard potential. Up to one year following shutdown the increase was by less than a factor of two. More importantly the increase in the activity produced by long-lived radioisotopes was by less than an order of magnitude, more than a hundred years after shutdown. These results do

not present any serious problems from the long-term radioactivity point of view, as these conservative values are more than two orders of magnitude less than the activity induced by fusion neutrons.

As a final conclusion, this study indicates that the fusion neutron-induced activity remains the dominant source of radioactivity in D-^{3}He fusion reactors.

Finally, a summary of suggestions for improvement of the analysis are given below.

1. Since the question of the level of accuracy of the proton cross section data used is always raised, a cross section sensitivity analysis might be desired assuming that the uncertainties in the experimental cross section data can be found in the literature. One might also take a look at the possibility of using one of the available nuclear model codes to calculate these cross sections.

2. The evaluation of the energy spectrum of neutrons produced by proton/structure (p,n) reactions can be enhanced as more of the experimentally measured angular distributions of the neutrons produced for intermediate and heavy elements become available. With this data, it would become possible to assume that the center of mass angular distribution is piecewise linear rather than the isotropic assumption used in this study. Another approach to evaluate the neutron energy spectrum

would be to use a nuclear model code (GNASH as an example) to calculate a differential neutron production cross section that describes the probability of neutron production at any given energy and direction.

However, the proton-induced radioactivity is shown to be significantly smaller than the radioactivity induced by the fusion neutrons such that considering the proposed suggestions are not expected to alter the conclusions reached in this thesis.

Bibliography

[1] A. P. Fraas and H. Postma, "Preliminary Appraisal of the Hazards Problems of a D-T Fusion Reactor Power Plant," *Oak Ridge National Laboratory*, **ORNL-TM-2822** (Apr.,1970, revised Nov.,1970).

[2] D. Steiner, "The Neutron-Induced Activity and Decay Power of the Niobium Structure of a D-T Fusion Reactor Blanket," *Oak Ridge National Laboratory*, **ORNL-TM-3094** (Aug., 1970).

[3] D. Steiner, "A Review of the ORNL Fusion Feasibility Studies," *Oak Ridge National Laboratory*, **ORNL-TM-3222** (Dec., 1970).

[4] D. Dudziak, "A Technical Note on D-T Fusion Reactor Afterheat," *Nuclear Technology*, **10**, 391 (1971).

[5] D. Steiner and A. P. Fraas, "Preliminary Observations on the Radiological Implications of Fusion Power," *Nuclear Safety*, **13, 5**, 353 (1972).

[6] A. P. Fraas, "Conceptual Design of the Blanket and Shield Region and Related Systems for a Full Scale Toroidal Fusion Reactor," *Oak Ridge National Laboratory*, **ORNL-TM-3096** (May, 1973).

[7] J. Powell, *et al.*, "Minimum Activity Blankets for Commercial and Experimental Power Reactors," *Brookhaven National Laboratory*, **BNL-18439** (Nov., 1973).

[8] J. R. Powell, "Preliminary Reference Design of Fusion Reactor Blanket Exhibiting Very Low Residual Radioactivity," *Brookhaven National Laboratory*, **BNL-19565** (Dec., 1974).

[9] G. L. Kulcinski, R. G. Lott and T. Yang, "Transmutation Effects in CTR Materials," *University of Wisconsin*, **UWFDM-42** (March, 1973).

[10] W. F. Vogelsang, *et al.*, "Transmutation, Radioactivity and Afterheat in a D-T Tokamak Fusion Reactor," *Nuclear Technology*, **22**, 379 (1974).

[11] W. G. Price, "D-T Fusion Reactor Activation and Afterheat," *Transactions of American Nuclear Society*, **19**, 459 (1974).

[12] D. J. Dudziak and R. A. Krakowski, "Radioactivity Induced in a Theta-Pinch Fusion Reactor," *Nuclear Technology*, **25**, 32 (1975).

[13] R. W. Conn, *et al.*, "New Concepts for Controlled Fusion Reactor Blanket Design," *Nuclear Technology*, **26**, 125 (1975).

[14] R. W. Conn, T. Y. Sung and M. A. Abdou, "Comparative Study of Radioactivity and Afterheat in Several Fusion Reactor Blanket Designs," *Nuclear Technology*, **26**, 391 (1975).

[15] M. L. Williams, R. T. Santoro and T. A. Gabriel, "The Calculated Performance of Various Structural Materials in Fusion Reactor Blankets," *Nuclear Technology*, **29**, 384 (1976).

[16] W. F. Vogelsang, "Radioactivity and Associated Problems in Thermonuclear Reactors," *University of Wisconsin*, **UWFDM-178** (Sept., 1976).

[17] E. T. Cheng, T. Y. Sung and D. K. Sze, "Neutronics Studies of the Gas-Carried Lithium Oxide Cooling-Breeding Fusion Reactor Blanket and Shield," *Nuclear Technology*, **34**, 362 (1977).

[18] R. W. Conn, K. Okula and A. W. Johnson, "Minimizing Radioactivity and Other Features of Elemental and Isotopic Tailoring of Materials for Fusion Reactors," *Nuclear Technology*, **41**, 389 (1978).

[19] M. Z. Youssef and R. W. Conn, "Induced Radioactivity and Influence of Materials Selection in Deuterium-Deuterium and Deuterium-Tritium Fusion Reactors," *Nuclear Technology/Fusion*, **3**, 361 (1983).

[20] H. Attaya, *et al.*, "Activation Characteristics of Different Steel Alloys Proposed for Near-Term Fusion Reactors," *Fusion Technology*, **15**, **2**, **2B**, 893 (1989).

[21] H. Y. Khater, *et al.*, "Activation Analysis for the Aqueous Self-Cooled Blanket and Shield of ITER," *Fusion Technology*, **15, 2, 2B**, 900 (1989).

[22] W. F. Vogelsang and H. Y. Khater, "The Impact of D-^{3}He Fusion Reactors on Waste Disposal," *Fusion Engineering and Design*, **5, 4**, 367 (1988).

[23] J. F. Santarius, *et al.*, "Ra: A High Efficiency, D-^{3}He Tandem Mirror Fusion Reactor," *University of Wisconsin*, **UWFDM-741** (Oct., 1987).

[24] G. L. Kulcinski, *et al.*, "Apollo - An Advanced Fuel Fusion Power Reactor for the 21st Century," to be Published in *Fusion Technology* (March, 1989), or *University of Wisconsin*, **UWFDM-780** (Oct., 1988).

[25] J. Jung, "Theory and Use of the Radioactivity Code RACC," *Argonne National Laboratory*, **ANL/FPP/TM-122** (1979).

[26] J. Jung, "Multigroup Neutron Activation Cross Section Library RACCXLIB and Decay Chain Library RACCDLIB for the Radioactivity Calculation Code RACC," *Argonne National Laboratory*, to be published.

[27] D. Garber, "ENDF/B Summary Documentation," *Brookhaven National Laboratory*, **BNL-17541** (1975).

[28] W. B. Ewbank and M. R. Schmorak, "Evaluated Nuclear Structure Data File; A Manual for Preparation of Data Sets," *Oak Ridge National Laboratory*, **ORNL-5054/R1** (1977).

[29] F. M. Mann, "Transmutation of Alloys In MFE Facilities as Calculated by REAC (A Computer Code System for Activation and Transmutation)," *Hanford Engineering Development Laboratory*, **HEDL-TME 81-37** (1982).

[30] R. L. Bunting and C. W. Reich, "Evaluation Procedures for Experimental Data," Proceedings of the Conference on Nuclear Data Evaluation Methods and Procedures," *Brookhaven National Laboratory*, **BNL-NCS-51363** (1981).

[31] C. M. Lederer and V. S. Shirley, "Table of Isotopes," 7th ed., *John Wiley & Sons, Inc.*, New York (1978).

[32] J. A. Blink, "FORIG: A Modification of the ORIGEN2 Isotope-Generation and Depletion Code for Fusion Problems," *Lawerence Livermore National Laboratory*, **UCRL-53263** (1982).

[33] A. G. Croff, "A User's Manual for the ORIGEN2 Computer Code," *Oak Ridge National Laboratory*, **ORNL-TM-7175** (1980).

[34] M. J. Bell, "ORIGEN: The ORNL Isotope Generation and Depletion Code," *Oak Ridge National Laboratory*, **ORNL-4628** (1973).

[35] J. A. Blink, R. E. Dye and J. R. Kimlinger, "ORLIB: A Computer Code that Produces One-Energy Group, Time - and Spatially-Averaged Neutron Cross Section," *Lawerence Livermore National Laboratory*, **UCRL-53262** (1981).

[36] M. A. Gardner and R. J. Howerton, "ACTL: Evaluated Neutron Activation Cross Section Library - Evaluation Techniques and Reaction Index," *Lawerence Livermore National Laboratory*, **UCRL-50400, Vol. 18** (1978).

[37] E. F. Plechaty and J. R. Kimlinger, "TARTNP: A Coupled Neutron-Photon Monte Carlo Transport Code," *Lawerence Livermore National Laboratory*, **UCRL-50400, Vol. 14** (1976).

[38] T. Y. Sung and W. F. Vogelsang, "DKR: A Radioactivity Calculation Code for Fusion Reactors," *University of Wisconsin*, **UWFDM-170** (Sept., 1976).

[39] T. Y. Sung and W. F. Vogelsang, "Decay Chain Data Library for Radioactivity Calculations," *University of Wisconsin*, **UWFDM-171** (Sept., 1976).

[40] D. L. Henderson and O. Yasar, "DKR-ICF: A Radioactivity and Dose Rate Calculation Code Package," *University of Wisconsin*, **UWFDM-714, Vol. 1** (Apr., 1987).

[41] A. M. White, "Transmutation and Activation Analysis of Fusion Power Plants," Ph.D. Thesis, *University of Wisconsin - Madison* (1985).

[42] R. S. Tilbury, "Activation Analysis with Charged Particles," *National Academy of Sciences, National Research Council*, **NAS-NS-3110** (1976).

[43] G. Friedlander, J. Kennedy and J. Miller, "Nuclear and Radiochemistry," *John Wiley & Sons, Inc.*, New York (1964).

[44] N. N. Krasnov, "Thick Target Yield," *International Journal of Applied Radiation and Isotopes*, **25**, 223 (1974).

[45] K. Svoboda, "Terms Used in the Production of Radioisotopes by Charged-Particle Bombardment," *The Use of Cyclotrons in Chemistry, Metallurgy and Biology*, **P. 383**, Butterworths, London (1970).

[46] J. Lange and H. Münzel, "Estimation of Unknown Excitation Functions for (xn), (pxn), (d,xn), (d,pxn) and (p,xn) Reactions," *Kernforschungszentrum Karlsruhe*, **KFK-767** (May, 1968).

[47] N. N. Krasnov, "Physical Principles of Activation Analysis with Charged Particles," *Atomnaya Energiya*, **26, 3**, 284 (1969).

[48] K. A. Keller, J. Lange and H. Münzel, "Numerical Data and Functional Relationships in Science and Technology," *Landölt- Bornstein, New Series*, **Vol. I/5C**, Springer (1974).

[49] R. Mather and E. Segre, "Range Energy Relation for 340-MeV Protons," *Physical Review*, **84, 2**, 191 (1951).

[50] M. Z. Maksimov, "Range Energy Relation for Some Substances," *Zh. Eksper. Teoret. Fiz.*, **37**, 127 (1959).

[51] B. V. Robuch and A. Gentilini, "Proton-Nuclide Reaction Cross Sections a Collection of Data from Literature," *Comitato Nazionale Per La Ricerca E Per Lo Sviluppo Dell'Energia Nucleare E Delle Energie Alternative*, **RT/FUS/87/31** (1987).

[52] H. Münzel *et al.*, "Karlsruhe Charged Particle Reaction Data Compilation," *Fachinformationszentrum Karlsruhe*, **Physics Data, No. 15** (1982).

[53] National Nuclear Data Center, "On-Line Data Bases," *Brookhaven National Laboratory.*

[54] H. H. Anderson and J. F. Ziegler, "HYDROGEN Stopping Powers and Ranges in All Elements," *Pergamon Powers*, New York (1977).

[55] E. Amaldi, "Neutrons and Related Gamma Ray Problems," *Encyclopedia of Physics*, **Vol. 38/2, P. 90**, Springer-Verlag, Berlin (1959).

[56] S. T. Perkins, "Multigroup Transfer Matrices for Charged-Particle and Neutron-Induced Reactions. Part I: The General Two-Body Interaction," *Nuclear Science and Engineering*, **80**, 130 (1982).

[57] S. T. Perkins, "Multigroup Transfer Matrices for Charged-Particle and Neutron-Induced Reactions. Part II: An Analytic Integration of the Inner Integral," *Nuclear Science and Engineering*, **80**, 579 (1982).

[58] R. J. Howerton, R. E. Dye and S. T. Perkins, "Evaluated Nuclear Data Library," *Lawerence Livermore National Laboratory*, **UCRL-50400, Vol. 4, Rev. 1** (1981).

[59] M. Abramowitz and I. A. Stegun, Eds., "Handbook of Mathematical Functions," *National Bureau of Standards*, **AMS-55** (1964).

[60] S. T. Perkins, "An Exact Benchmark Calculation for l'th Mode Multigroup Transfer Matrix Analysis," *Nuclear Science and Engineering*, **82**, 115 (1982).

[61] G. L. Kulcinski *et al.*, "Apollo - L2 An Advanced Fuel Tokamak Reactor Utilizing Direct Conversion," *Proceedings of the IEEE 13 th Symposium on Fusion Engineering*, **pp. 1043-1046**, Knoxville, TN. (1989).

[62] J. F. Santarius, Private Communication (1990).

[63] R. O'Dell, *et al.*, "User's Manual for ONEDANT: A Code Package for One-Dimensional, Diffusion-Accelerated, Neutral Particle Transport," *Los Alamos National Laboratory*, **LA-9184-M** (1982).

[64] H. Y. Khater, "WDR: A Code for Radwaste Classification," unpublished.

[65] H. Chow *et al.*, "ATHENA Code Manual," *EG&G Idaho Report*, **RST7034, Vol. 1 Draft** (1985).

[66] D. Smith *et al.*, "Blanket Comparison and Selection Study," *Argonne National Laboratory*, **ANL/FPP/TM-122** (1984).

[67] Nuclear Regulatory Commission, 10CFR part 61, "Licensing Requirements for Land Disposal of Radioactive Waste," *Federal Register*, **FR 47**, 57446 (1982).

[68] S. Fetter, E. Cheng and F. Mann, "Long Term Radioactivity in Fusion Reactors," *Fusion Engineering and Design*, **Vol. 6**, pp. 123-130 (1988).

[69] H. Y. Khater *et al.*, "Activation and Safety Analyses for the D-^{3}He Fueled Tokamak Reactor Apollo," *Proceedings of the IEEE 13 th Symposium on Fusion Engineering*, **pp. 728-731**, Knoxville, TN. (1989).